IOP Publishing Inverse Problems

Inverse Problems **35** (2019) 055003 (29pp) https://doi.org/10.1088/1361-6420/ab0ccd

Theory of the linear sampling method for time-dependent fields

Aaron C Prunty and Roel K Snieder

Department of Geophysics, Colorado School of Mines, Golden, CO, United States of America

E-mail: prunty@mines.edu

Received 15 July 2018, revised 22 February 2019
Accepted for publication 5 March 2019
Published 2 May 2019

Abstract

The linear sampling method seeks to localize the unknown source of an observed, time-dependent field. The unknown source could be, for example, a scatterer embedded within a medium, or an impulsive excitation such as an earthquake or explosion. The source of the observed field is localized by means of solving the so-called *near-field equation* and mapping the obtained solutions through an indicator functional over a test region assumed to contain the source. In its current formulation, however, the linear sampling method suffers from an ambiguous time parameter that strongly influences its ability to localize the unknown source. Our paper consists of two fundamental results central to the theoretical understanding of the linear sampling method and its numerical implementation. First, we prove the so-called *blowup behavior* of solutions to the near-field equation for a general source function that is separable in space and time. Second, we show that the linear sampling method can be formulated such that the ambiguous time parameter is irrelevant. We demonstrate that a dependence of the linear sampling method on the time parameter arises from an incorrect implementation of a convolution-type operator found in the near-field equation. When the operator is implemented correctly, the dependence on the time parameter vanishes. We provide detailed algorithms for efficient and proper implementations of the convolutional operator in both the time and frequency domains. The crucial result of the improved implementations is that they allow the linear sampling method to be completely automated, as one does not need to know the space-time dependence of the unknown source. We demonstrate the effectiveness of the improved time- and frequency-domain implementations using several numerical examples applied to imaging scatterers.

Keywords: linear sampling method, inverse scattering, focusing, time domain

(Some figures may appear in colour only in the online journal)

1. Introduction

The linear sampling method [1–4] is an inverse scattering technique that aims to localize the unknown source of an observed field. First introduced as a way to image scattering objects using monochromatic waves, the method relates the measured far-field patterns of the scattered waves to that of an impulse response of the host medium in which the scattering object is embedded. The impulse response is the wave field generated by a hypothesized source localized at a particular *sampling point* in the host medium. In particular, the far-field patterns of the scattered waves and impulse response are related through an ill-posed integral equation called the *far-field equation*. The effectiveness of the linear sampling method in reconstructing the support of a scatterer relies on a characteristic *blowup behavior* of solutions to the far-field equation. In particular, the norm of a solution becomes arbitrarily large whenever the sampling point lies outside the support of the scatterer. This behavior has been studied and rigorously proven for the far-field case (e.g. [5, 6] and the references therein).

Due to the limited spatial resolution provided by a single frequency, the quality of the obtained reconstructions using monochromatic waves is relatively poor. Consequently, efforts to improve the accuracy of the linear sampling method have been made more recently [7–9]. By interrogating the scatterer with signals that possess a continuous range of frequencies, the accuracy of the reconstructed targets is significantly enhanced. In this approach, the linear sampling method relates time-domain recordings of near-field scattered waves to an impulse response of the host medium through the *near-field equation*. Although the desired blowup behavior of solutions to the near-field equation has yet to be rigorously proven (a task that is considerably more difficult than for the far-field case), several numerical experiments have validated the blowup behavior (e.g. [8, 9]). With the time-domain approach, however, came an ambiguous time parameter that strongly influences the ability of the method to faithfully reconstruct the support of the scatterer. In particular, the literature to date indicates that 'an appropriate time shift' must be chosen to obtain an image of the scatterer [7–10], yet no information is offered on how this parameter should be chosen. We have found that a clear and precise analysis of the time parameter and its influence on the reconstruction process has yet to be provided.

In this paper, we give a simple proof of the blowup behavior of solutions to the near-field equation, and show that a proper formulation of the linear sampling method can be obtained without introducing an ambiguous time parameter. We find that the reported dependence on the time parameter arises when a discretized convolutional operator found in the near-field equation is truncated. When the full convolution is implemented correctly, the dependence on the time parameter vanishes. Moreover, we present an algorithm for solving the near-field equation in the frequency domain, in which the recorded signals have sparse representations, that substantially reduces computational cost compared to the time-domain approach.

In what follows, we provide a brief overview of the time-domain linear sampling method, introducing relevant equations, definitions, and parameters (section 2). We then present a physical framework in which to formulate the linear sampling method, and in particular to prove the blowup behavior of solutions to the near-field equation (appendix) and analyze the role of the time parameter (section 3). Next, we provide an in-depth discussion on the numerical solution of the near-field equation, with a particular emphasis on how to properly and efficiently implement the convolutional operator in both the time and frequency domains (section 4). Following this discussion, we present several numerical examples applied to imaging scatterers to demonstrate the effectiveness of the improved implementations (section 5). We conclude our paper by examining a few implications of our proof of the blowup behavior for other possible applications of the linear sampling method, as well as the performance of the improved algorithms (section 6).

2. Overview of the time-domain linear sampling method

In this section, we present an overview of the time-domain linear sampling method as is typically done for the case of imaging a scatterer. For simplicity, we consider the scattering of acoustic waves due to an inhomogeneity of compact support $D \subset \mathbb{R}^3$. The generalization to elastic wave scattering is relatively straightforward and has been considered in [10], for example. We assume the inhomogeneity is modeled by a variable wave speed $c = c(\mathbf{x})$, with $c(\mathbf{x}) > 0$ for all $\mathbf{x} \in D$, and that the wave speed is a positive constant $c = c_0$ for all $\mathbf{x} \in \mathbb{R}^3 \setminus \overline{D}$, where $\overline{D}$ denotes the closure of D. For a point source located at $\mathbf{x}_s \in \mathbb{R}^3$, let u be the total wave that satisfies the initial-value problem

$$\nabla^2 u(\mathbf{x}, t) - \frac{1}{c^2(\mathbf{x})} \frac{\partial^2 u(\mathbf{x}, t)}{\partial t^2} = -\delta(\mathbf{x} - \mathbf{x}_s)\chi(t), \qquad \mathbf{x} \in \mathbb{R}^3, \quad t > 0, \tag{1a}$$

$$u(\mathbf{x}, t) = 0, \qquad \frac{\partial u(\mathbf{x}, t)}{\partial t} = 0, \qquad \mathbf{x} \in \mathbb{R}^3, \quad t \leqslant 0, \tag{1b}$$

where δ is the Dirac delta distribution and $\chi \in C^2(\mathbb{R})$ is a time-dependent function that describes the shape of the wave.

The total wave can be decomposed into an incident wave u^i and a scattered wave u^s such that $u = u^i + u^s$ is a solution to (1*a*) and (1*b*). By defining the *refractive index*

$$n(\mathbf{x}) := \frac{c_0^2}{c^2(\mathbf{x})},$$

and the *contrast function*

$$m := 1 - n, \tag{2}$$

it follows that if the incident wave u^i satisfies

$$\nabla^2 u^i(\mathbf{x}, t) - \frac{1}{c_0^2} \frac{\partial^2 u^i(\mathbf{x}, t)}{\partial t^2} = -\delta(\mathbf{x} - \mathbf{x}_s)\chi(t), \quad \mathbf{x} \in \mathbb{R}^3, \quad t > 0, \tag{3a}$$

$$u^i(\mathbf{x}, t) = 0, \qquad \frac{\partial u^i(\mathbf{x}, t)}{\partial t} = 0, \quad \mathbf{x} \in \mathbb{R}^3, \quad t \leqslant 0, \tag{3b}$$

then the scattered wave u^s satisfies

$$\nabla^2 u^s(\mathbf{x}, t) - \frac{1}{c_0^2} n(\mathbf{x}) \frac{\partial^2 u^s(\mathbf{x}, t)}{\partial t^2} = -\frac{1}{c_0^2} m(\mathbf{x}) \frac{\partial^2 u^i(\mathbf{x}, t)}{\partial t^2}, \quad \mathbf{x} \in \mathbb{R}^3, \quad t > 0,$$

$$u^s(\mathbf{x}, t) = 0, \qquad \frac{\partial u^s(\mathbf{x}, t)}{\partial t} = 0, \qquad \mathbf{x} \in \mathbb{R}^3, \quad t \leqslant 0.$$

The unique solution to (3*a*) and (3*b*) is given by the convolution of the free-space Green function (i.e. the radiating fundamental solution) with the pulse function χ:

$$u^i(\mathbf{x}, t; \mathbf{x}_s) := \frac{\chi(t - c_0^{-1}|\mathbf{x} - \mathbf{x}_s|)}{4\pi|\mathbf{x} - \mathbf{x}_s|}. \tag{4}$$

In an imaging experiment, we record the total wave field u at receiver locations $\mathbf{x}_r$, which are typically restricted to an acquisition surface we denote by Γ_r. Similarly, the sources used to generate the wave field u are restricted to points $\mathbf{x}_s$ of an acquisition surface we denote

by Γ_s (possibly equal to Γ_r) such that Γ_s and $\overline{D}$ are disjoint. Consequently, we can consider constructing an incident wave generated by a distribution of sources over Γ_s. Such an incident wave is given by a linear combination of expression (4):

$$v_\varphi(\mathbf{x},t) := \int_{\mathbb{R}}\int_{\Gamma_s} \frac{\chi(t-t_s-c_0^{-1}|\mathbf{x}-\mathbf{x}_s|)}{4\pi|\mathbf{x}-\mathbf{x}_s|}\varphi(\mathbf{x}_s,t_s)\,\mathrm{d}s(\mathbf{x}_s)\,\mathrm{d}t_s, \tag{5}$$

where $\varphi \in L^2(\Gamma_s \times \mathbb{R})$ is a spatiotemporal *density function*. The definition given in expression (5) defines a *Herglotz wave function*. Since v_φ is an incident wave, it follows by linearity that the function

$$w_\varphi(\mathbf{x},t) := \int_{\mathbb{R}}\int_{\Gamma_s} u^s(\mathbf{x},t-t_s;\mathbf{x}_s)\varphi(\mathbf{x}_s,t_s)\,\mathrm{d}s(\mathbf{x}_s)\,\mathrm{d}t_s \tag{6}$$

is a radiating solution to

$$\nabla^2 w_\varphi(\mathbf{x},t) - \frac{1}{c_0^2}n(\mathbf{x})\frac{\partial^2 w_\varphi(\mathbf{x},t)}{\partial t^2} = -\frac{1}{c_0^2}m(\mathbf{x})\frac{\partial^2 v_\varphi(\mathbf{x},t)}{\partial t^2}, \quad \mathbf{x}\in\mathbb{R}^3, \quad t\in\mathbb{R}.$$

Thus, w_φ is a scattered wave. When the scattered wave u^s is evaluated on the receiver surface Γ_r, expression (6) defines the *near-field operator* $\mathcal{N} : L^2(\Gamma_s \times \mathbb{R}) \to L^2(\Gamma_r \times \mathbb{R})$ by setting $w_\varphi = \mathcal{N}\varphi$.

Finally, we introduce a prescribed wave function $\Psi_{\mathbf{z},\tau} = \Psi(\mathbf{x}, t-\tau;\mathbf{z})$, often called a *test function*, which is the impulse response of the host medium due to a point source localized at $\mathbf{z}\in\mathbb{R}^3$ and at time $\tau\in\mathbb{R}$:

$$\Psi(\mathbf{x},t-\tau;\mathbf{z}) := \frac{\zeta(t-\tau-c_0^{-1}|\mathbf{x}-\mathbf{z}|)}{4\pi|\mathbf{x}-\mathbf{z}|}. \tag{7}$$

Here, $\zeta \in C^2(\mathbb{R})$ is a time-dependent function with compact support. The test function (7) represents a wave field that can be computed based on the assumption that the host medium (in this case, the constant wave speed c_0) is known. We note that this test function is often assigned the same time dependence $\chi \in C^2(\mathbb{R})$ as the incident wave (4) that interrogates the scatterer (as was done in [7–11]). This choice is typically valid in an active imaging experiment in which the sources distributed over Γ_s are known (as opposed to a passive imaging experiment in which unknown, ambient sources generate the interrogating waves), and is often simply made for convenience. If the time dependence of the generating source function is unknown, then ζ should be chosen such that it possesses the same frequency band as the observed signals (the reason for this requirement will be explained in section 4). Since we are analyzing the linear sampling method in the context of an active imaging experiment, we assume the sources distributed over Γ_s are known, and in particular that their time dependence is given by the known function χ. Hence, we follow our predecessors and choose $\zeta = \chi$.

The linear sampling method treats the functions (v_φ, w_φ) as an incident-scattered wave pair of an inverse focusing problem [12]. In particular, the goal of the linear sampling method is to find a spatiotemporal density function $\varphi_{\mathbf{z},\tau} \in L^2(\Gamma_s \times \mathbb{R})$ such that scattered wave $w_{\varphi_{\mathbf{z},\tau}}$, as observed on the receiver surface Γ_r, coincides with a prescribed test function $\Psi_{\mathbf{z},\tau}$; that is, we set $w_{\varphi_{\mathbf{z},\tau}} = \Psi_{\mathbf{z},\tau}$ on Γ_r and, using the definition of the near-field operator $\mathcal{N}$, solve the ill-posed integral equation

$$\mathcal{N}\varphi_{\mathbf{z},\tau} = \Psi_{\mathbf{z},\tau} \tag{8}$$

in a least-squares sense. Equation (8) is called the *near-field equation*. Provided we can separate the scattered wave u^s from the total wave u recorded on Γ_r (via the difference $u^s = u - u^i$), we can solve the near-field equation to obtain a density function $\varphi_{\mathbf{z},\tau}$ such that the constructed Herglotz wave function $v_{\varphi_{\mathbf{z},\tau}}$ optimally focuses onto the point $\mathbf{z}$ at time τ, and $w_{\varphi_{\mathbf{z},\tau}} = \Psi_{\mathbf{z},\tau}$ is the resulting scattered wave.

An interesting comparison can be made between the time-domain linear sampling method and the well-established time reversal method [13–15] as focusing techniques. In the time reversal method, an impulsive source generates a wave that propagates through an inhomogeneous medium and is recorded on an acquisition surface. The observed signals are then time-reversed and re-emitted into the original medium, now acting as a source-time function distributed over the recording surface. Such an acquisition surface is called a *time-reversal mirror* (TRM). In particular, the time reversal method requires that the medium be invariant to time reversal, and that Γ_r and Γ_s be coincident. Thus, the time reversal method is best suited for lossless, nonattenuating media. By modifying how the time-reversed signals are re-emitted into the original medium, the time reversal method can focus the observed field onto a strongly scattering target or the location of the impulsive source. In contrast, the linear sampling method does not rely on time-reversal invariance of the wave equation to achieve focusing, nor does it require that Γ_r and Γ_s be coincident. Consequently, the linear sampling method can be applied to weakly attenuating media, or even to diffusive fields. (Note that the functions v_φ and $\Psi_{\mathbf{z},\tau}$—given by expressions (5) and (7), respectively—require knowledge of the host medium for their computation. If we mistakenly assume the host medium is lossless, then the corresponding errors will be absorbed into the solution to the near-field equation (8). In this case, we expect a degraded accuracy in the obtained reconstructions. However, if the attenuation in a medium is so strong that no waves are observed, then clearly the linear sampling method will fail. In this case, we would obtain a trivial (zero) near-field operator, and every solution to equation (8) would lie in its null space.) Perhaps most interesting, the focusing of the Herglotz wave function $v_{\varphi_{\mathbf{z},\tau}}$ onto the sampling point $\mathbf{z}$ does not depend on a knowledge of the target scatterer. This can be seen from the definition of $v_{\varphi_{\mathbf{z},\tau}}$ given by expression (5), which depends only on the density function $\varphi_{\mathbf{z},\tau}$ obtained by solving equation (8), and the known incident field u^i that propagates through the host medium without the scatterer. We will expand our discussion of how the Herglotz wave function focuses in section 3.

We can obtain an image of the scatterer by exploiting the *blowup behavior* of the solutions $\varphi_{\mathbf{z},\tau}$, which is generally described by $\|\varphi_{\mathbf{z},\tau}\|_{L^2(\Gamma_s\times\mathbb{R})} < \infty$ for $\mathbf{z} \in D$ and $\|\varphi_{\mathbf{z},\tau}\|_{L^2(\Gamma_s\times\mathbb{R})} \to \infty$ for $\mathbf{z} \in \mathbb{R}^3 \setminus \overline{D}$. In particular [7–9], if $\mathbf{z} \in D$ we have the limiting behavior

$$\lim_{\mathbf{z}\to\partial D} \|\varphi^\alpha_{\mathbf{z},\tau}\|_{L^2(\Gamma_s\times\mathbb{R})} = \infty,$$

where ∂D denotes the boundary of D, and for all $\mathbf{z} \in \mathbb{R}^3 \setminus \overline{D}$ we have

$$\lim_{\alpha\to 0} \|\varphi^\alpha_{\mathbf{z},\tau}\|_{L^2(\Gamma_s\times\mathbb{R})} = \infty,$$

where $\alpha > 0$ is a regularization parameter and $\varphi^\alpha_{\mathbf{z},\tau}$ denotes a regularized solution to the near-field equation (8). Thus, the norm $\|\varphi_{\mathbf{z},\tau}\|_{L^2(\Gamma_s\times\mathbb{R})}$ effectively behaves as a binary indicator for the support of the scatterer. Note that since Γ_s and $\overline{D}$ are disjoint, the norm $\|\varphi_{\mathbf{z},\tau}\|_{L^2(\Gamma_s\times\mathbb{R})}$ remains unbounded as $\mathbf{z}$ approaches Γ_s. However, as stated in section 1, it is not well understood based on the literature to date how the norm $\|\varphi_{\mathbf{z},\tau}\|_{L^2(\Gamma_s\times\mathbb{R})}$ behaves as τ is varied. This ambiguity in the time parameter must be addressed and corrected if the linear sampling method is to see its use in practical applications concerning time-dependent fields.

Traditionally, the point $\mathbf{z}$ in space is called a *sampling point*, a term used since the inception of the linear sampling method for the scattering of monochromatic waves. In the next section,

we present a physical framework in which the time parameter τ can be viewed as the fourth component to a four-dimensional *space-time sampling point*. Within this framework, we relate the sampling point $(\mathbf{z}, \tau)$ to the focusing point and focusing time of the inverse scattering problem. We provide physical arguments that set clear limitations on the values that τ can assume based on the time interval over which the data are recorded.

3. Space-time, causality, and the sampling of the near-field operator

Waves are generated by sources that depend on both space and time. When the evolution of the waves through a medium is time invariant, this statement can be written compactly as

$$u = G_0 \circledast S, \tag{9}$$

where G_0 is the unperturbed Green function of the background medium (which in general may be inhomogeneous), S is a source function, and $\circledast$ denotes integration over space and convolution in time. Implicitly captured in expression (9) is the notion of causality, in which the support of the wave u in space-time is determined by the support of the functions G_0 and S. Intuitively, the source function S determines from which points in space-time the waves originate, and the Green function G_0 describes how the waves propagate away from those points.

For the purpose of illustration, consider the space-time diagram shown in figure 1(a), which shows the propagation of a wave $u = u^i + u^s$ in a one-dimensional medium consisting of two scatterers (shown as the dark gray circles to the left of the space axis). The scattered wave u^s (shown in green) is recorded in a time interval $[t_0, t_f] \subset \mathbb{R}$, which has length $T = t_f - t_0$. In this example, the scatterers can be thought of as a secondary source function that generates the scattered wave u^s. Using expression (9), we can write the scattered wave u^s as the wave generated by this secondary source function, say S', so that $u^s = G_0 \circledast S'$. The support of S' (shown in blue) is localized in space by the locations of the scatterers, whereas the support of S' in time is determined by the travel times of all the waves incident to the scatterers. In this illustration, the total wave incident to the scatterers consists of the incident wave u^i and all the reverberations between the scatterers.

Figure 1(b) illustrates the convolution of the scattered waves u^s in the near-field equation. Here, we prescribe a test function $\Psi_{\mathbf{z},\tau}$ (shown in red), which is the wave field generated by a source localized in space-time at the sampling point $(\mathbf{z}, \tau)$. The near-field equation (8) attempts to construct the prescribed test function $\Psi_{\mathbf{z},\tau}$ from a linear combination of the scattered waves u^s. In particular, $\Psi_{\mathbf{z},\tau}$ is set to be a *convolution* of the scattered waves u^s. Consequently, the scattered waves u^s are time-reversed, shifted, and integrated with an unknown function $\varphi_{\mathbf{z},\tau}$ such that $\Psi_{\mathbf{z},\tau}$ is the resulting convolution. Since $\Psi_{\mathbf{z},\tau}$ is defined to be a singular radiating wave, clearly $\varphi_{\mathbf{z},\tau}$ must act as an inverse of the source function S' (otherwise $\Psi_{\mathbf{z},\tau}$ would contain multiple wave arrivals). The solution to the near-field equation $\varphi_{\mathbf{z},\tau}$ thus contains the time shifts and scattering amplitudes necessary to construct a Herglotz wave function $v_{\varphi_{\mathbf{z},\tau}}$ that focuses onto the sampling point $(\mathbf{z}, \tau)$. That is, the Herglotz wave function is constructed in such a way as to 'cancel' its interactions with the scatterers as it propagates through the medium. As can be seen from figure 1(b), the solution $\varphi_{\mathbf{z},\tau}$ can effectively cancel the unknown source function S' if the time-reversed scattered waves can be shifted so that the sampling point $(\mathbf{z}, \tau)$ lies within the support of S'. That is, $\varphi_{\mathbf{z},\tau}$ is an effective inverse of S' if and only if the point $\mathbf{z}$ lies within the support of the source function S' along the space axis. If $\mathbf{z}$ lies within the support of S', we say the sampling point $\mathbf{z}$ is *causal*, since at this point in space there was a causal (or physical) source of scattered waves. Otherwise, we say the sampling point is *acausal*.

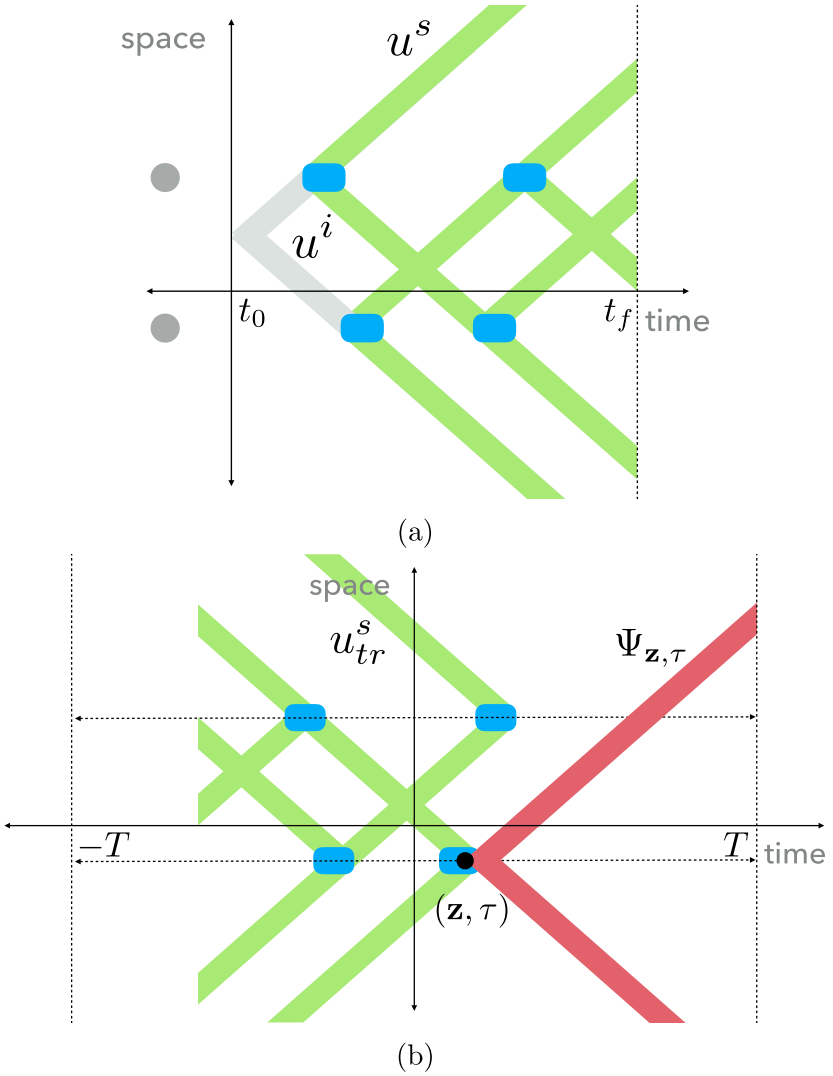

Figure 1. One-dimensional space-time diagrams illustrating (a) the forward scattering problem and (b) the linear sampling method. An unknown source function S' (shown in blue) generates the scattered waves u^s. A prescribed sampling point $(\mathbf{z},\tau)$ determines from which point in space-time the test function $\Psi_{\mathbf{z},\tau}$ (shown in red) propagates. When the point $\mathbf{z}$ lies within the support of S' along the space axis, the time-reversed scattered waves u^s_{tr} can be shifted so that the sampling point $(\mathbf{z},\tau)$ lies within the support of S'.

Note that the time axis in figure 1(b) spans the *convolution interval* $[-T,T]$— *not* the physical time interval $[t_0,t_f]$ in which the data are recorded. This is due to the fact that the incident and scattered waves of the inverse focusing problem (v_φ,w_φ) are *convolutions* of the incident and scattered waves of the forward scattering problem (u^i,u^s), respectively. For the near-field equation to be consistent, the prescribed test functions $\Psi_{\mathbf{z},\tau}$ must also be evaluated over the convolution interval $[-T,T]$. Here, τ is a *focusing time*; i.e. a time at which the Herglotz wave function $v_{\varphi_{\mathbf{z},\tau}}$ focuses onto the point $\mathbf{z}$ and the test function $\Psi_{\mathbf{z},\tau}$ radiates. It follows that the length of the recording interval T has two important consequences. First, the accuracy of the

convolution of the scattered wave u^s is directly dependent on how well u^s is represented in the recording interval. In particular, if the support of the scattered wave u^s is effectively contained in the recording interval $[t_0, t_f]$, then we can expect its convolution w_φ to have compact support in the interval $[-T, T]$. Second, the near-field equation has a nontrivial solution only when the test function $\Psi_{\mathbf{z},\tau}$ lies in the convolution interval $[-T, T]$, as observed on a given recording surface Γ_r. For a fixed recording length T, a focusing time τ can always be found such that the test function $\Psi_{\mathbf{z},\tau}$ (at least partially) lies in the convolution interval $[-T, T]$. That is, no matter how near or far the point $\mathbf{z}$ is from the recording surface Γ_r, the test functions can be shifted in time to lie in the interval $[-T, T]$. Thus, the size of the sampling region (or imaging domain) is arbitrary.

Provided we have adequately recorded the scattered wave u^s, consider the sampling points $\mathbf{z}$ for which the test functions $\Psi_{\mathbf{z},\tau}$ fully lie in the convolution interval $[-T, T]$ when $\tau = 0$. In this case, the observed test functions $\Psi_{\mathbf{z}}$ are nonzero only in the subinterval $[0, T]$, which has the same length as the recording interval $[t_0, t_f]$. Clearly, the source of the observed field must lie in this region of space, since both the test functions and the data are contained in a time interval of the same length as measured on the recording surface Γ_r. For these sampling points, the near-field equation will have nontrivial solutions, and an image of the source function can therefore be obtained. Note, however, that the test functions will not lie in the interval $[-T, T]$ for $\tau \geqslant T$, and generally for $\tau \ll -T$. For these values of τ, the near-field equation will have trivial solutions, and the linear sampling method will fail. Hence, provided the observed field is adequately contained in the recording interval, the parameter τ can be discarded (i.e. set to zero) without loss of generality.

We now show how sampling the near-field operator $\mathcal{N}$ generates solutions to the near-field equation with the desired blowup behavior. We give a proof in the appendix for a general source function that is separable in space and time, and apply the result here for the case of localizing a scatterer. According to the Lippmann–Schwinger equation [16], the scattered wave u^s has the integral representation

$$u^s(\mathbf{x}, t; \mathbf{x}_s) = -\frac{1}{c_0^2} \int_{\mathbb{R}} \int_D G_0(\mathbf{x}, t - t'; \boldsymbol{\eta}) m(\boldsymbol{\eta}) \frac{\partial^2 u(\boldsymbol{\eta}, t'; \mathbf{x}_s)}{\partial t'^2} \, \mathbf{d}\boldsymbol{\eta} \, \mathrm{d}t',$$

where m is the contrast function (2) with compact support D and $u(\cdot, \cdot, \mathbf{x}_s)$ is the total wave incident to the scatterer due to a source at $\mathbf{x}_s \in \Gamma_s$. Note that the scattered wave u^s has the form of expression (9) if we identify $S = mu_{tt}$. Such a source function is called a *contrast source*. Following the procedure given in the appendix, we find that the near-field equation can be rewritten as

$$\int_{\mathbb{R}} \int_{\Gamma_s} \frac{\partial^2 u(\mathbf{z}, t - t'; \mathbf{x}_s)}{\partial t'^2} \varphi(\mathbf{x}_s, t') \, \mathrm{d}s(\mathbf{x}_s) \, \mathrm{d}t' = -\frac{c_0^2 \zeta(t)}{m(\mathbf{z})}, \quad \mathbf{z} \in D. \tag{10}$$

It follows that in the limit as $\mathbf{z} \to \partial D$, the contrast function $m(\mathbf{z}) \to 0$ and the right-hand side of equation (10) becomes unbounded. In fact, by definition (2), the contrast function $m(\mathbf{z}) = 0$ for all $\mathbf{z} \in \mathbb{R}^3 \setminus \overline{D}$. Thus, any solution $\varphi_{\mathbf{z}}$ to equation (10)—and consequently to the near-field equation (8)—becomes unbounded as $\mathbf{z} \to \partial D$, and remains unbounded for all $\mathbf{z} \in \mathbb{R}^3 \setminus \overline{D}$. Thus, the blowup behavior of solutions to the near-field equation is due to division by the contrast function m with compact support D.

The behavior of $\|\varphi_{\mathbf{z}}\|_{L^2(\Gamma_s \times \mathbb{R})}$ has a simple physical interpretation [12]. The L^2 norm of each solution $\varphi_{\mathbf{z}}$ is effectively a measure of the energy required to construct a singular, radiating wave from a linear combination of the recorded data u^s that originated from the sampling point $\mathbf{z}$. In other words, we can use expression (9) to write the near-field equation as

$$u^s \circledast \varphi_{\mathbf{z}} = \Psi_{\mathbf{z}},$$

so that $\varphi_{\mathbf{z}}$ can be thought of as a type of *inverse source function*, and its L^2 norm as a measure of its energy. We saw above that sampling the near-field operator is equivalent to sampling the source function that generates the observed field. If the sampling point $\mathbf{z}$ is causal (that is, if $\mathbf{z}$ is inside the scatterer), then the recorded data contain the field u^s due to that source point in space. In this case, the linear sampling method matches the energy of the test function $\Psi_{\mathbf{z}}$ with the energy of the scattered waves u^s due to the source point $\mathbf{z}$. Since the recorded data have finite energy, the energy of the source function $\varphi_{\mathbf{z}}$ is finite. Otherwise, if the sampling point is acausal, then there is no corresponding field in the recorded data that can be attributed to the sampling point $\mathbf{z}$. Here, the linear sampling method reasonably predicts that the amount of energy required to construct the test function $\Psi_{\mathbf{z}}$ is infinite, because it takes a source function $\varphi_{\mathbf{z}}$ of infinite energy to construct $\Psi_{\mathbf{z}}$ from waves that never existed.

Regarding the numerical solution of the near-field equation, the common mistake found in the literature to date is to truncate the convolution to fit within a support which has the same length as the recorded time interval. As we show in the next section, truncating the convolution discards much of the information provided by the scattered wave u^s, and negatively impacts the ability of the linear sampling method to localize the unknown source. In this case, the focusing time τ becomes crucial to ensure that the prescribed test functions $\Psi_{\mathbf{z},\tau}$ lie in a particular subset of the interval $[-T, T]$. The particular subset of $[-T, T]$ needed to obtain an accurate image is determined by which part of the convolution is truncated.

4. On the numerical solution of the near-field equation

In this section, we give an in-depth discussion on the numerical implementation of the near-field operator in both the time and frequency domains, including detailed algorithms. As we will show, the frequency-domain implementation is more economical in many cases than the time-domain implementation, especially when the signals are band-limited. First, we briefly describe a general procedure for setting up a least-squares formulation of the ill-posed near-field equation. Our strategy is to apply a Tikhonov regularization scheme [17] and obtain a least-squares solution to

$$\min_{\boldsymbol{\varphi}_{\mathbf{z},\tau}} \|\mathbf{N}\boldsymbol{\varphi}_{\mathbf{z},\tau} - \boldsymbol{\Psi}_{\mathbf{z},\tau}\|_2^2 + \alpha\|\boldsymbol{\varphi}_{\mathbf{z},\tau}\|_2^2 \tag{11}$$

for the time-domain case and

$$\min_{\hat{\boldsymbol{\varphi}}_{\mathbf{z}}} \|\hat{\mathbf{N}}\hat{\boldsymbol{\varphi}}_{\mathbf{z}} - \hat{\boldsymbol{\Psi}}_{\mathbf{z}}\|_2^2 + \alpha\|\hat{\boldsymbol{\varphi}}_{\mathbf{z}}\|_2^2 \tag{12}$$

for the frequency-domain case. Here, $\alpha \geqslant 0$ is the regularization parameter. For the frequency-domain case, the parameter τ is taken to be zero. The discretized near-field operator is given in the time domain by

$$(\mathbf{N}\boldsymbol{\varphi})(i,k) := \sum_{l=-N_t+1}^{N_t-1} \sum_{j=1}^{N_s} u^s(\mathbf{x}_i, (k-l)\Delta t; \mathbf{y}_j)\boldsymbol{\varphi}(j,l)$$

and in the frequency domain by

$$(\hat{\mathbf{N}}\hat{\boldsymbol{\varphi}})(i;\boldsymbol{\omega}) := \sum_{j=1}^{N_s} \hat{u}^s(\mathbf{x}_i, \mathbf{y}_j; \boldsymbol{\omega})\hat{\boldsymbol{\varphi}}(j;\boldsymbol{\omega}),$$

where $i = 1, \ldots, N_r$, where N_r is the number of receivers; $j = 1, \ldots, N_s$, where N_s is the number of sources; and $k = -N_t + 1, \ldots, N_t - 1$, where N_t is the number of time samples used to record the scattered wave u^s and Δt is the length of a time step. Note that for the time-domain case we do not limit k and l to the interval $[1, N_t]$, which would be valid only if the nonzero durations of *both* u^s and $\boldsymbol{\varphi}$ are known to be limited to the interval $[1, N_t]$. Since $\boldsymbol{\varphi}$ is unknown, we do not make this assumption. Here, $\boldsymbol{\omega}$ is a vector of angular frequencies which is determined by a user-specified bandpass filter. Similarly, the discretized test functions are given in the time and frequency domains by

$$\boldsymbol{\Psi}_{\mathbf{z},\tau}(i,k) = \Psi_{\mathbf{z},\tau}(\mathbf{x}_i, k\Delta t)$$

and

$$\hat{\boldsymbol{\Psi}}_{\mathbf{z}}(i;\boldsymbol{\omega}) = \hat{\Psi}_{\mathbf{z}}(\mathbf{x}_i;\boldsymbol{\omega}),$$

respectively. We follow the general approach of [8, 9] and obtain least-squares solutions to equations (11) and (12) using a truncated singular-value decomposition (SVD) of the discretized near-field operators $\mathbf{N}$ and $\hat{\mathbf{N}}$, respectively. As is often noted in the literature, the singular-value decomposition is aptly suited for the linear sampling method—since the scattered wave u^s is independent of any sampling point $(\mathbf{z}, \tau) \in \mathbb{R}^3 \times \mathbb{R}$, the singular-value decomposition of $\mathbf{N}$ (or $\hat{\mathbf{N}}$) is independent of any sampling point as well, and therefore need only be computed once. Hence, an efficient approach to the linear sampling method consists of two main steps: (1) estimate a low-rank approximation to the discretized near-field operator via a truncated SVD; and (2) approximate the solutions to (11) and (12) for each sampling point by orthogonally projecting the test functions onto the solution space using the SVD. We denote by $(\sigma_n, \boldsymbol{\phi}_n, \boldsymbol{\psi}_n)$ the singular-value decomposition of $\mathbf{N}$, where σ_n are the singular values and $\boldsymbol{\phi_n}$ and $\boldsymbol{\psi}_n$ are the corresponding left- and right-singular vectors, respectively. Similarly, we denote by $(\sigma_n, \hat{\boldsymbol{\phi}}_n, \hat{\boldsymbol{\psi}}_n)$ the singular-value decomposition of $\hat{\mathbf{N}}$. Using the K largest singular values and corresponding vectors [18], an approximate solution is computed for each sampling point as

$$\tilde{\boldsymbol{\varphi}}^{\alpha}_{\mathbf{z},\tau} = \sum_{n=1}^{K} \frac{\sigma_n}{\alpha + \sigma_n^2} (\boldsymbol{\phi}_n \cdot \boldsymbol{\Psi}_{\mathbf{z},\tau}) \boldsymbol{\psi}_n \tag{13}$$

for the time-domain case and as

$$\tilde{\boldsymbol{\varphi}}^{\alpha}_{\mathbf{z}} = \sum_{n=1}^{K} \frac{\sigma_n}{\alpha + \sigma_n^2} (\hat{\boldsymbol{\phi}}_n \cdot \hat{\boldsymbol{\Psi}}_{\mathbf{z}}) \hat{\boldsymbol{\psi}}_n \tag{14}$$

for the frequency-domain case. Note that if the chosen pulse function $\zeta \in C^2(\mathbb{R})$ does not possess the same frequency band as the recorded data, then the projections $\boldsymbol{\phi}_n \cdot \boldsymbol{\Psi}_{\mathbf{z},\tau}$ and $\hat{\boldsymbol{\phi}}_n \cdot \hat{\boldsymbol{\Psi}}_{\mathbf{z}}$ are trivially zero, since the singular vectors will lie in a frequency band disjoint from that of the test functions. Consequently, the obtain solutions $\tilde{\boldsymbol{\varphi}}^{\alpha}_{\mathbf{z}}$ are trivially zero. Hence, it is important to analyze the frequency content of the recorded data before choosing the pulse function ζ.

An image is obtained by mapping the obtained solutions (13) and (14) through an *indicator functional* $\mathcal{I}$ that assigns to each sampling point $(\mathbf{z}, \tau)$ a value based on the norm of the solution (recall $\tau = 0$ for the frequency-domain case). We define the indicator function as

$$\mathcal{I}(\mathbf{z}, \tau) := \frac{f(\mathbf{z}, \tau) - \min_{\mathbf{z}} f(\mathbf{z}, \tau)}{\max_{\mathbf{z}} f(\mathbf{z}, \tau) - \min_{\mathbf{z}} f(\mathbf{z}, \tau) + \epsilon},$$

where

$$f(\mathbf{z},\tau) := \frac{1}{\|\tilde{\varphi}^{\alpha}_{\mathbf{z},\tau}\|_2 + \epsilon}.$$

Here, the norm of $\tilde{\varphi}^{\alpha}_{\mathbf{z},\tau}(j,l)$ is computed over all $j = 1,\ldots,N_s$ and $l = -N_t+1,\ldots,N_t-1$ (or $l = 1,\ldots,N_\omega$ in the frequency domain where N_ω is the number of frequency samples). We have added a small positive number ϵ—typically taken to be the *machine precision* of the computer—to the denominator of each term for numerical stability. Thus, by the blowup behavior of the solutions (13) and (14), we have $0 \leqslant \mathcal{I}(\mathbf{z},\tau) \leqslant 1$, where values close to zero indicate an 'unlikely' location of the source function and values close to one indicate a 'likely' location of the source function.

The question remains on how to efficiently obtain a truncated SVD of the discretized near-field operators $\mathbf{N}$ and $\hat{\mathbf{N}}$. As noted in [8, 9], an efficient way to do this is by estimating the actions of $\mathbf{N}$ and $\hat{\mathbf{N}}$ through the use of so-called *matrix-vector products* that define their forward and adjoint operations. These matrix-vector products then define a linear operator whose SVD can be estimated using open-source software packages such as ARPACK [19]. As we discuss next, how we define these matrix-vector products significantly affects the accuracy of the obtained SVD. In particular, we focus on the effects of truncating the convolution in the near-field operator and how this leads to a dependence of the imaging algorithm on the time parameter τ.

4.1. Algorithms for an efficient implementation of the near-field operator

Our goal is to define matrix-vector products for the forward and adjoint operations of the discretized near-field operators $\mathbf{N}$ and $\hat{\mathbf{N}}$. According to the well-known convolution theorem, convolution in the time domain is equivalent to multiplication in the frequency domain. Hence, the convolution in the near-field operator $\mathbf{N}$ can be performed using a fast Fourier transform algorithm (FFT), which is most efficient for signals of length 2^n for some natural number $n \in \mathbb{N}$. We can further increase efficiency by using an FFT algorithm that exploits the fact that the recorded data are real valued, in which case the Fourier transform is conjugate symmetric with respect to the positive and negative frequencies.

Let $\mathbf{D} \in \mathbb{R}^{N_r \times N_t \times N_s}$ denote a three-dimensional array consisting of the sampled scattered wave u^s, so that $\mathbf{D}(i,k,j) = u^s(\mathbf{x}_i, k\Delta t; \mathbf{x}_j)$. As stated in section 3, the common mistake in the literature to date is to truncate the convolution in the discretized near-field operator $\mathbf{N}$ so that it has the same length N_t as the data array $\mathbf{D}$. To see the significance of this mistake, we refer to figure 2, which illustrates the convolution of two arbitrary signals in both the time and frequency domains. In the middle row of figure 2, the convolution in the time domain has length $2N_t - 1$. The highlighted regions indicate two possible subintervals of length N_t that are returned in a truncated implementation of the discretized near-field operator $\mathbf{N}$. In general, a subinterval of length N_t is insufficient to capture the full convolution. Hence, truncation of the convolution discards much of the information provided by the scattered wave u^s. This is equivalent to *under-representing* the discretized near-field operator $\mathbf{N}$. Intuitively, truncation of the convolution manifests in a singular-value decomposition as a more rapid decay of the singular values, since a truncated convolutional operator contains 'less' information than an operator that returns a full convolution.

The bottom row of figure 2 shows the amplitude spectrum of one of the convolved signals in the frequency domain. Because the signal is band-limited, its representation in the frequency domain is sparse. Hence, the convolution in the frequency domain will be nonzero only where the two signals being convolved have overlapping support. This is shown in the bottom right panel of figure 2, where the full convolution in the frequency domain lies in a small subset of the total frequency range needed to represent the convolution in the time domain. Hence, we

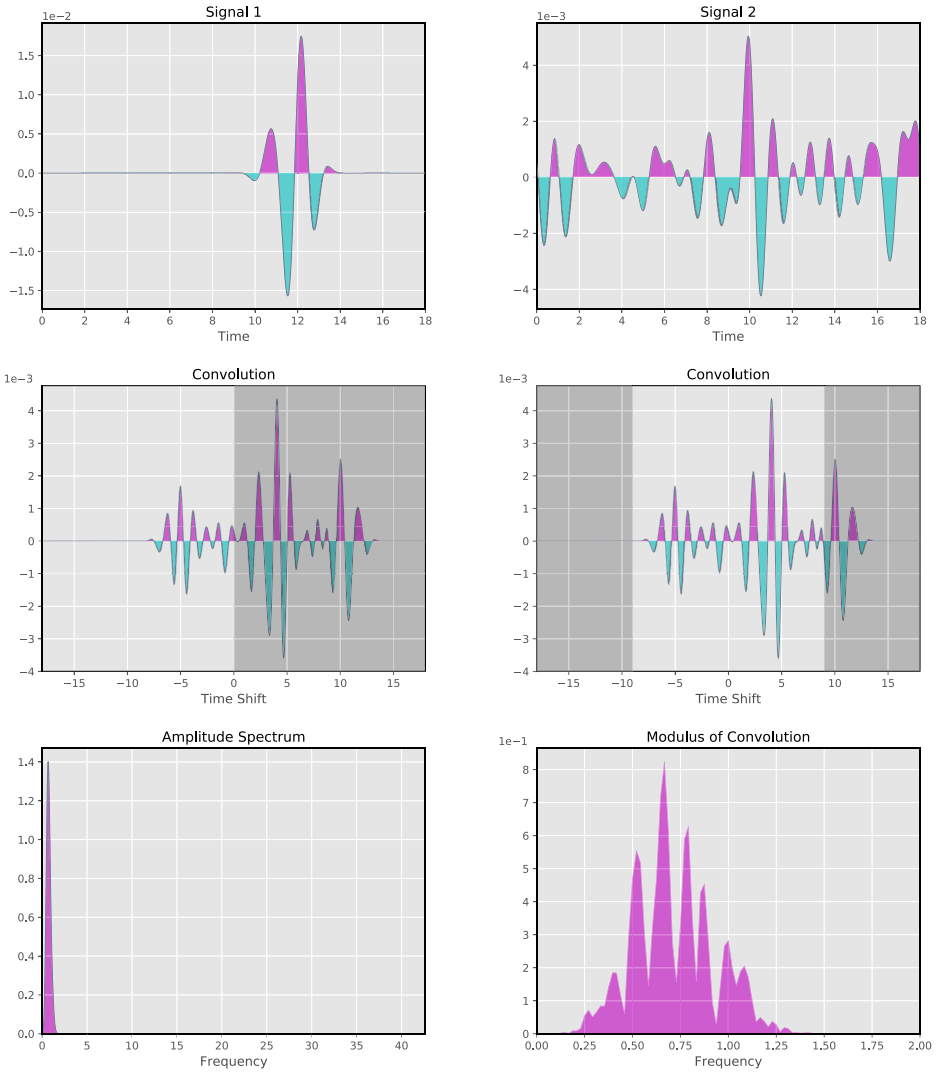

Figure 2. Two signals of length N_t and their convolution. *Middle row*: The convolution in the time domain has length $2N_t - 1$. The highlighted regions indicate two possible subintervals of length N_t that are returned in a truncated implementation of the discretized near-field operator. *Bottom row*: (left) The amplitude spectrum of signal 1 based on the $2N_t - 1$ samples needed to represent the convolution in the time domain. (right) The support of the convolution in the frequency domain lies in a small subinterval of length $M \ll 2N_t - 1$.

can exploit the sparseness of the convolution in the frequency domain to obtain a discretized convolutional operator that is significantly smaller than its equivalent representation in the time domain. To do this, we can simply apply a bandpass filter to the data array $\mathbf{D}$ that covers the support of the recorded signals in the frequency domain. When the signals are well sampled in the recorded time interval (that is, for sufficiently large N_t), the filtered data array in the frequency domain will typically have a length $M \ll 2N_t - 1$.

Algorithms 1 and 2 provide detailed procedures for implementing the discretized near-field operators $\mathbf{N}$ and $\hat{\mathbf{N}}$, respectively. Both implementations share a common first step of padding the

data array $\mathbf{D}$ with zeros to the end of its time axis so that its new length is the next power of two greater than the length of the convolution $2N_t - 1$. Next, a forward FFT is applied once to the extended data array along its time axis. In algorithms 1 and 2, we use H to denote the Hermitian transpose and the notation desc $:A \to B$ to represent a transformation, where 'desc' is a brief descriptor of what the transformation does. To obtain low-rank approximations of $\mathbf{N}$ and $\hat{\mathbf{N}}$, we define two functions that perform their forward and adjoint operations, which we name '*forward*' and '*adjoint*', respectively, in algorithms 1 and 2. These two functions are then used to define a linear operator, whose SVD can then be estimated for the K largest singular values and corresponding vectors. We note that in algorithm 1, the convolution computed in the frequency domain as length N, but the transformation back to the time domain returns only the first $2N_t - 1$ samples. Because we initially zero-pad the *end* of the time axis of the data array $\mathbf{D}$, the full convolution lies in the first $2N_t - 1$ samples of the computed convolution. Note that the total number of forward and inverse FFT operations performed in algorithm 1 is $N_r + N_s + 3$, while algorithm 2 performs just one forward FFT.

Algorithm 1. (Time domain).

set $N = 2^n$ such that $N > 2N_t - 1$
fft: $\mathbf{D} \in \mathbb{R}^{N_r \times N_t \times N_s} \to \hat{\mathbf{D}} \in \mathbb{C}^{N_r \times N \times N_s}$

def forward($\mathbf{x}$):
  reshape $\mathbf{x}$:
  $\mathbf{x} \in \mathbb{R}^{(2N_t-1)N_s \times 1} \to \mathbf{x} \in \mathbb{R}^{(2N_t-1) \times N_s}$
  fft: $\mathbf{x} \in \mathbb{R}^{(2N_t-1) \times N_s} \to \hat{\mathbf{x}} \in \mathbb{C}^{N \times N_s}$
  initialize $\mathbf{y} = \mathbf{0} \in \mathbb{R}^{(2N_t-1) \times N_r}$
  for $i = 1{:}N_r$
    $\hat{\mathbf{c}} = \hat{\mathbf{D}}(i, \cdot, \cdot)\hat{\mathbf{x}}$
    ifft: $\hat{\mathbf{c}} \in \mathbb{C}^{N \times N_s} \to \mathbf{c} \in \mathbb{R}^{(2N_t-1) \times N_s}$
    sum over sources:
    $\mathbf{y}(\cdot, i) = \text{sum}(\mathbf{c}, \text{axis} = 2)$
  reshape $\mathbf{y}$:
  $\mathbf{y} \in \mathbb{R}^{(2N_t-1) \times N_r} \to \mathbf{y} \in \mathbb{R}^{(2N_t-1)N_r \times 1}$
  return $\mathbf{y}$

def adjoint($\mathbf{y}$):
  reshape $\mathbf{y}$:
  $\mathbf{y} \in \mathbb{R}^{(2N_t-1)N_r \times 1} \to \mathbf{y} \in \mathbb{R}^{(2N_t-1) \times N_r}$
  fft: $\mathbf{y} \in \mathbb{R}^{(2N_t-1) \times N_r} \to \hat{\mathbf{y}} \in \mathbb{C}^{N \times N_r}$
  initialize $\mathbf{x} = \mathbf{0} \in \mathbb{R}^{(2N_t-1) \times N_s}$
  for $j = 1{:}N_s$
    $\hat{\mathbf{h}} = \hat{\mathbf{D}}(\cdot, \cdot, j)^H \hat{\mathbf{y}}$
    ifft: $\hat{\mathbf{h}} \in \mathbb{C}^{N \times N_r} \to \mathbf{h} \in \mathbb{R}^{(2N_t-1) \times N_r}$
    sum over receivers:
    $\mathbf{x}(\cdot, j) = \text{sum}(\mathbf{h}, \text{axis} = 2)$
  reshape $\mathbf{x}$:
  $\mathbf{x} \in \mathbb{R}^{(2N_t-1) \times N_s} \to \mathbf{x} \in \mathbb{R}^{(2N_t-1)N_s \times 1}$
  return $\mathbf{x}$

set $A = \text{LinearOperator}(\text{forward}, \text{adjoint})$
$\mathbf{U}, \mathbf{s}, \mathbf{V} = \text{svd}(A, K)$

Algorithm 2. (Frequency domain).

set $N = 2^n$ such that $N > 2N_t - 1$
fft: $\mathbf{D} \in \mathbb{R}^{N_r \times N_t \times N_s} \to \hat{\mathbf{D}} \in \mathbb{C}^{N_r \times N \times N_s}$
bandpass filter:
$\hat{\mathbf{D}} \in \mathbb{C}^{N_r \times N \times N_s} \to \tilde{\mathbf{D}} \in \mathbb{C}^{N_r \times M \times N_s}$

def forward($\hat{\mathbf{x}}$):
  reshape $\hat{\mathbf{x}}$:
  $\hat{\mathbf{x}} \in \mathbb{C}^{MN_s \times 1} \to \hat{\mathbf{x}} \in \mathbb{C}^{M \times N_s}$
  initialize $\hat{\mathbf{y}} = \mathbf{0} \in \mathbb{C}^{M \times N_r}$
    for $i = 1{:}N_r$
      $\hat{\mathbf{c}} = \tilde{\mathbf{D}}(i, \cdot, \cdot)\hat{\mathbf{x}}$
      sum over sources:
      $\hat{\mathbf{y}}(\cdot, i) = \text{sum}(\hat{\mathbf{c}}, \text{axis} = 2)$
    reshape $\hat{\mathbf{y}}$:
    $\hat{\mathbf{y}} \in \mathbb{C}^{M \times N_r} \to \hat{\mathbf{y}} \in \mathbb{C}^{MN_r \times 1}$
    return $\hat{\mathbf{y}}$

def adjoint($\hat{\mathbf{y}}$):
    reshape $\hat{\mathbf{y}}$:
    $\hat{\mathbf{y}} \in \mathbb{C}^{MN_r \times 1} \to \hat{\mathbf{y}} \in \mathbb{C}^{M \times N_r}$
    initialize $\hat{\mathbf{x}} = \mathbf{0} \in \mathbb{C}^{M \times N_s}$
    for $j = 1{:}N_s$
      $\hat{\mathbf{h}} = \tilde{\mathbf{D}}(\cdot, \cdot, j)^H \hat{\mathbf{y}}$
      sum over receivers:
      $\hat{\mathbf{x}}(\cdot, j) = \text{sum}(\hat{\mathbf{h}}, \text{axis} = 2)$
    reshape $\hat{\mathbf{x}}$:
    $\hat{\mathbf{x}} \in \mathbb{C}^{M \times N_s} \to \hat{\mathbf{x}} \in \mathbb{C}^{MN_s \times 1}$
    return $\hat{\mathbf{x}}$
set $\hat{A} = \text{LinearOperator(forward, adjoint)}$
$\hat{\mathbf{U}}, \mathbf{s}, \hat{\mathbf{V}} = \text{svd}(\hat{A}, K)$

5. Numerical examples

In this section, we perform several numerical examples applied to imaging scatterers to demonstrate the effectiveness of the improved time- and frequency-domain implementations of the discretized near-field operator compared to its truncated implementation. For the truncated implementation, we follow algorithm 1 with the exception that the first N_t samples of the computed convolution are returned in both the forward and adjoint operations. For the time-domain implementations, we test the dependence of the imaging algorithm for several values of the time parameter τ. In each example, the length of the recording interval T is specified. The test functions are evaluated in the time interval $[-T, T]$ for the for case of the full convolution, and in the interval $[0, T]$ for the case of the truncated convolution. For the frequency-domain implementation, we apply the same bandpass filter to the test functions as for the data array $\mathbf{D}$ in the computation of the SVD.

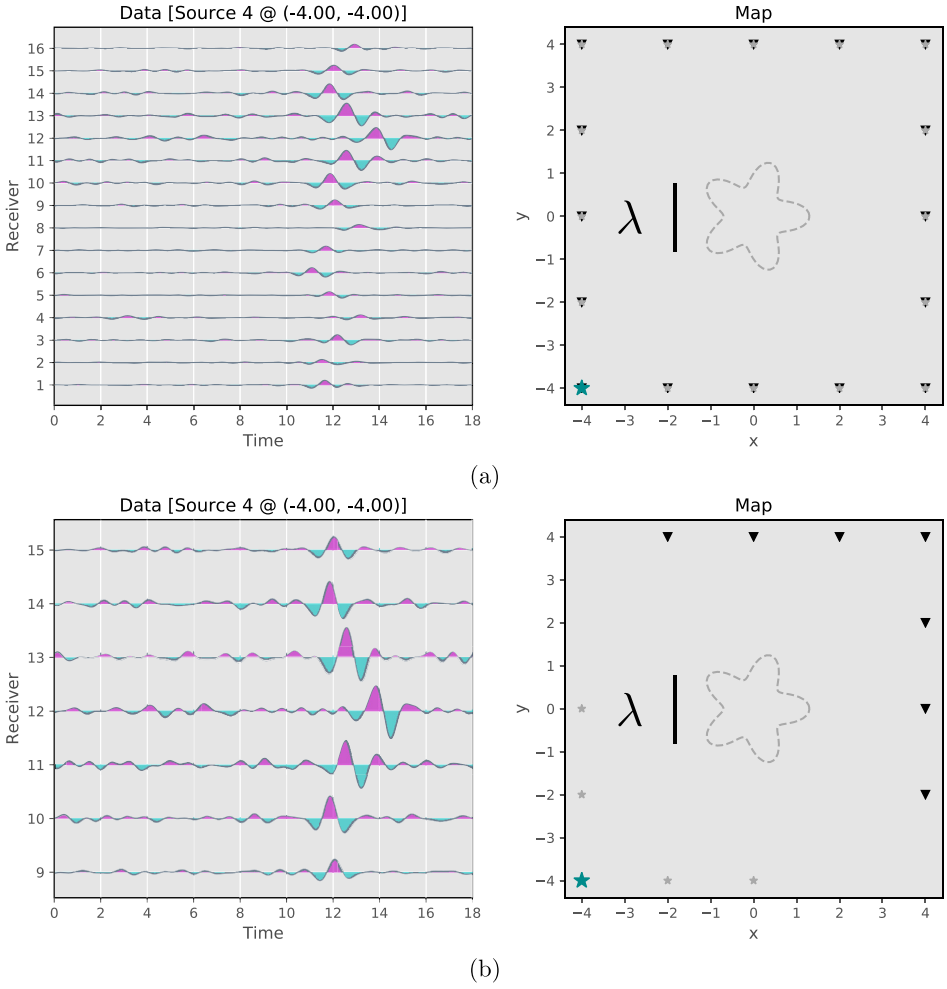

Figure 3. (a) The full-aperture imaging experiment and (b) the limited-aperture imaging experiment for the starfish-shaped scatterer. Sources are indicated by stars and receivers by triangles. The right panels show a map of the experiment indicating the particular source (large, cyan star) that generated the scattered data shown in the left panels. Band-limited white noise in the frequency range $[0.25, 1.25]$ has been added to the signals so that the computed SNR $= 4$.

For simplicity, we limit the numerical examples we present to the reconstruction of two-dimensional scatterers embedded within homogeneous background media. The method is easily generalized to three space dimensions and to inhomogeneous background media. Consequently, the test functions for all imaging experiments presented hereafter are computed as

$$\Psi_{\mathbf{z},\tau}(i,k) = \frac{\chi_{1,2}(k\Delta t - \tau - c_0^{-1}\|\mathbf{x}_i - \mathbf{z}\|_2)}{2\pi\sqrt{k^2\Delta t^2 - c_0^{-2}\|\mathbf{x}_i - \mathbf{z}\|_2^2} + \epsilon},$$

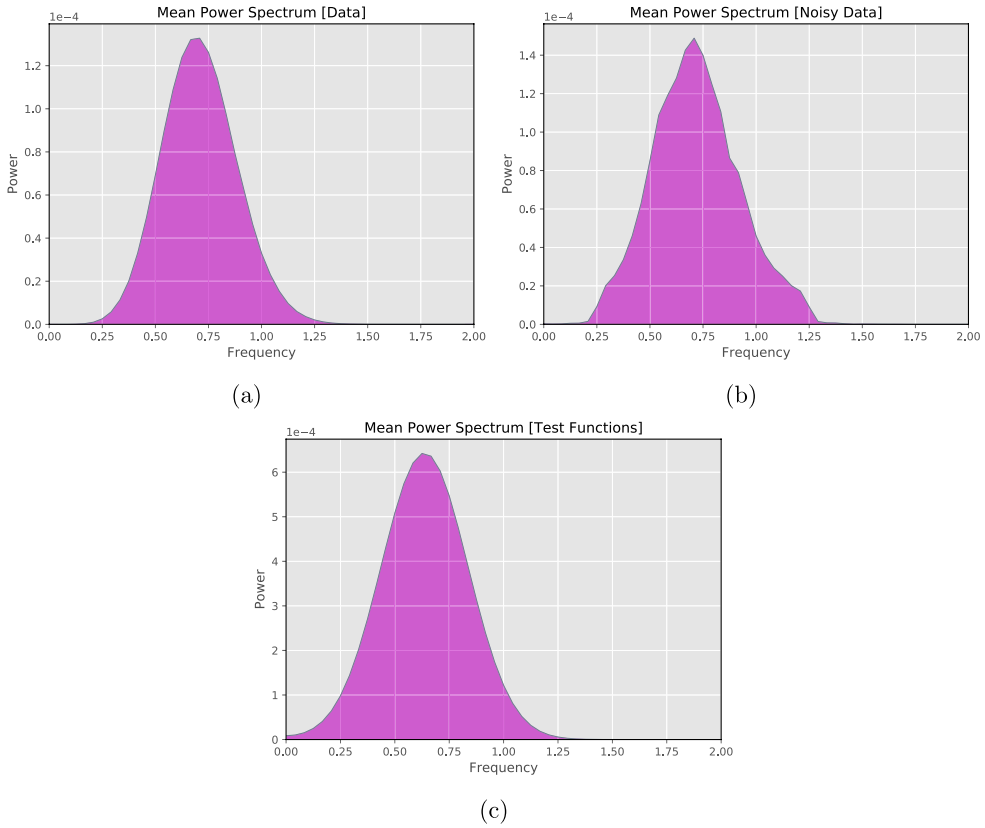

Figure 4. Power spectra for the starfish imaging experiment. The power spectrum is averaged over all recordings of the scattered wave for (a) the noise-free case and (b) after adding band-limited white noise in the frequency range $[0.25, 1.25]$ so that the computed $\mathrm{SNR} = 4$. (c) The mean power spectrum of the test functions with time dependence given by χ_1.

where the pulse functions $\chi_{1,2}$ are set to zero whenever their arguments are negative. We have again added the small positive number ϵ to the denominator for numerical stability. The pulse function is taken to be either

$$\chi_1(t) = \sin(4t)\mathrm{e}^{-1.6(t-3)^2}$$

or the Ricker pulse

$$\chi_2(t) = [1 - 2\pi^2\nu^2(t-0.1)^2]\mathrm{e}^{-\pi^2\nu^2(t-0.1)^2}.$$

All numerical computations are performed on a computer equipped with a 2.8 GHz quad-core Intel Core i7 processor and 16 GB of 1600 MHz DDR3 memory. The machine precision is $\epsilon = 2 \times 10^{-16}$. This parameter remains fixed throughout all numerical computations.

5.1. Starfish-shaped scatterer

Our first imaging experiment reconstructs a starfish-shaped scatterer using the same scattered wave and acquisition data as was used in [8]. In this case, the scatterer represents a

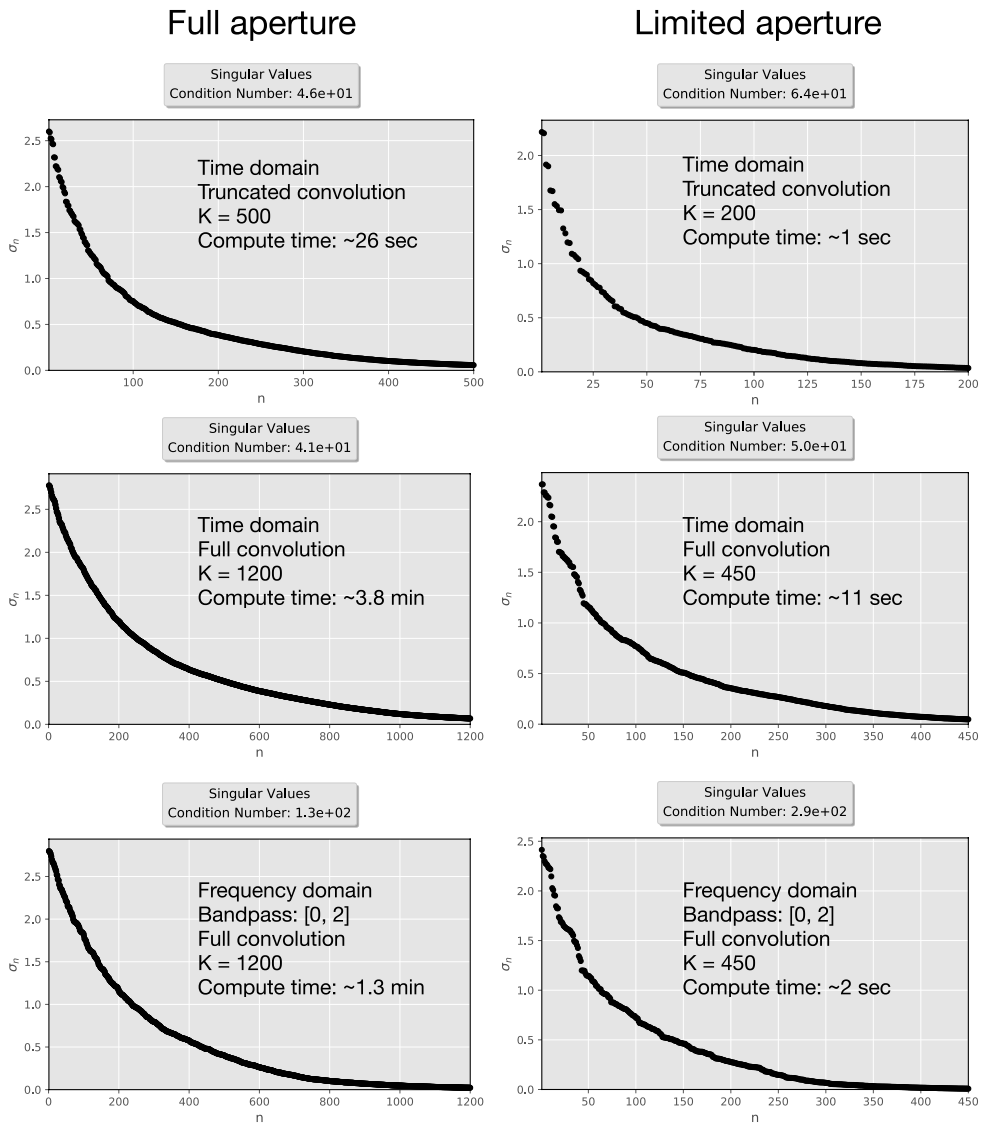

Figure 5. Estimated singular values for the full-aperture (left column) and limited-aperture (right column) imaging experiments for the starfish-shaped scatterer. Each column gives the estimated singular values based on the numerical implementation of the discretized near-field operator. The truncated convolution under-represents the discretized near-field operator, as evidenced by the more rapid decay of the singular values. The noisy data are used in all cases.

perturbation in the model wave speed, for which the background wave speed is $c_0 = 1$ and $c = 2$ inside the scatterer. We interrogate the scatterer under two different acquisition scenarios. In the first case, 16 sources and receivers are co-located around the scatterer, representing an ideal, full-aperture acquisition setup (figure 3(a)). In the second case, we place five sources in the lower-left corner below the scatterer and seven receivers in the upper-right corner above the scatterer, representing a limited-aperture acquisition setup that only measures transmitted

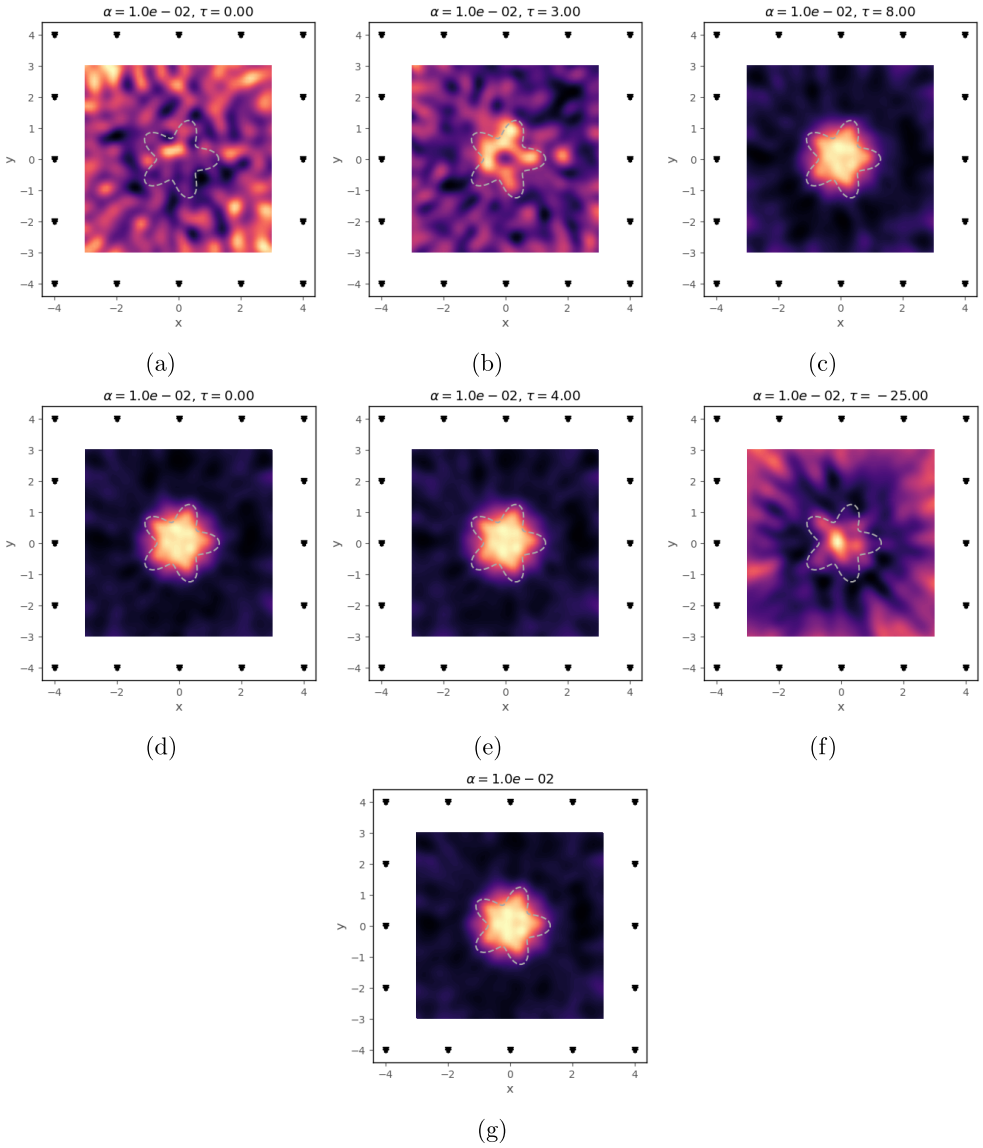

Figure 6. Reconstructions of the starfish-shaped scatterer for the full-aperture imaging experiment and noisy data with SNR $= 4$. ((a)–(c)) Reconstructions based on the truncated convolution in the time domain with $\tau = 0$, $\tau = 3$, and $\tau = 8$. ((d)–(f)) Reconstructions based on the full convolution in the time domain with $\tau = 0, \tau = 4$, and $\tau = -25$. When $\tau = -25$, the test functions partially lie outside the support $[-18, 18]$ and the method fails. (g) Reconstruction based on the frequency-domain approach. The regularization parameter $\alpha = 1 \times 10^{-2}$ in all cases.

waves (figure 3(b)). In both imaging experiments, we sample the model with a 61×61 point uniformly spaced sampling grid and interrogate the scatterer using the pulse function χ_1 (the dominant wavelength is shown in the right panels of figure 3 for scale). The scattered wave is recorded in the time interval $[0, 18]$ using a step size $\Delta t = 2.34 \times 10^{-2}$ for a total of $N_t = 769$ time samples. Consequently, the test functions are evaluated in the interval $[-18, 18]$ for the

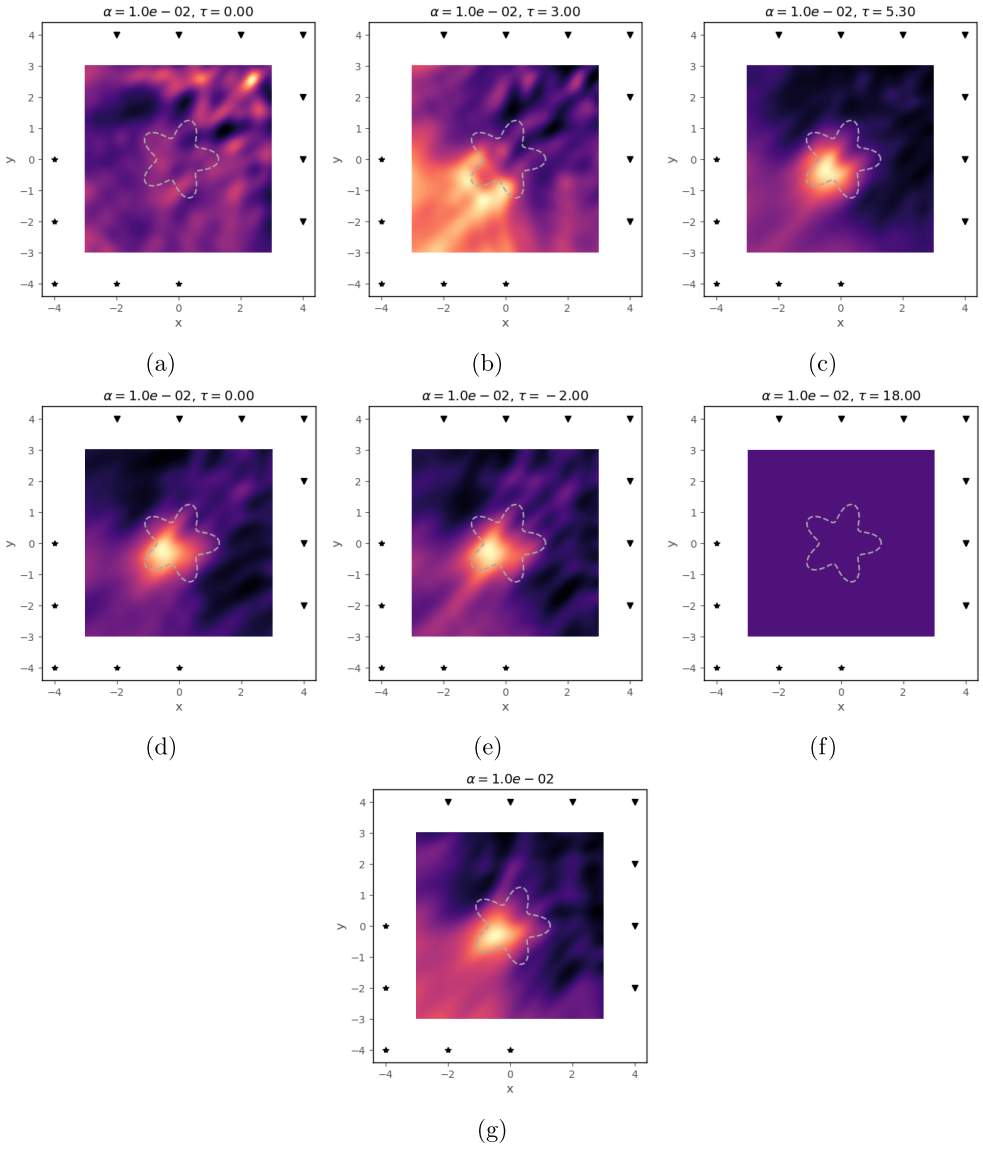

Figure 7. Reconstructions of the starfish-shaped scatterer for the limited-aperture imaging experiment and noisy data with SNR $= 4$. ((a)–(c)) Reconstructions based on the truncated convolution in the time domain with $\tau = 0$, $\tau = 3$, and $\tau = 5.3$. ((d)–(f)) Reconstructions based on the full convolution in the time domain with $\tau = 0$, $\tau = -2$, and $\tau = 18$. When $\tau = 18$, the test functions completely lie outside the support $[-18, 18]$ and the method fails. (g) Reconstruction based on the frequency-domain approach. The regularization parameter $\alpha = 1 \times 10^{-2}$ in all cases.

time- and frequency-domain implementations that use the full convolution, and in the interval $[0, 18]$ for the truncated implementation. The left panels of figure 3 show examples of the recorded scattered wave. To test the robustness of the imaging algorithm to noisy measurements, we add band-limited white noise in the frequency range $[0.25, 1.25]$ to the recorded data so that the computed signal-to-noise ratio (SNR) is 4, as defined by

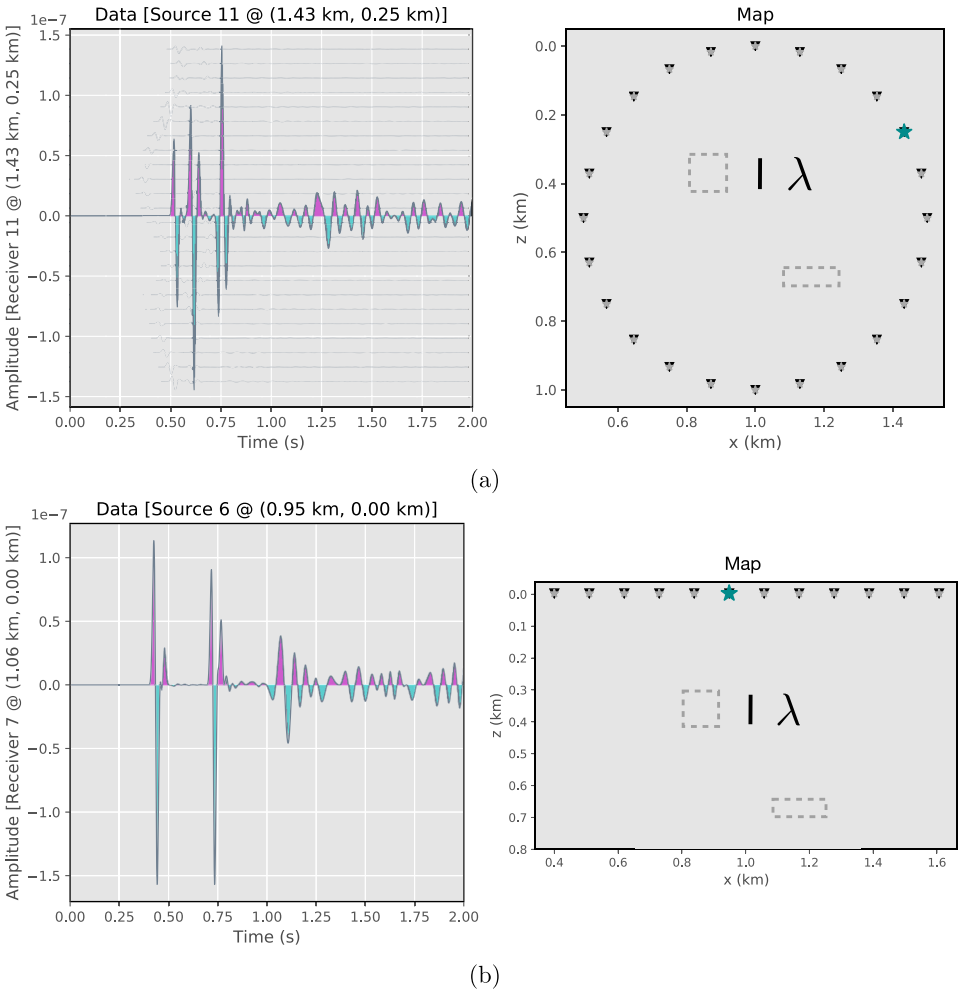

Figure 8. (a) The full-aperture imaging experiment and (b) the single-sided imaging experiment for the two box-shaped scatterers. Sources are indicated by stars and receivers by triangles. The right panels show a map of the experiment indicating the particular source (large, cyan star) that generated the scattered data shown in the left panels. No noise is added to the signals.

$$\text{SNR} := \frac{P_{\text{signal}}}{P_{\text{noise}}},$$

where P is the average power (i.e. the mean-square amplitude). The mean power spectrum of the recorded signals before and after adding the band-limited white noise is shown in figures 4(a) and 4(b), respectively, and the mean power spectrum of the test functions is shown in figure 4(c). Note that the frequency bands of the data and the test functions overlap significantly, as this ensures an optimal reconstruction of the target. Figure 5 shows the K largest singular values of the truncated SVD used to compute the time and frequency domain solutions (13) and (14), respectively. As we expect, the singular values decay faster for the truncated

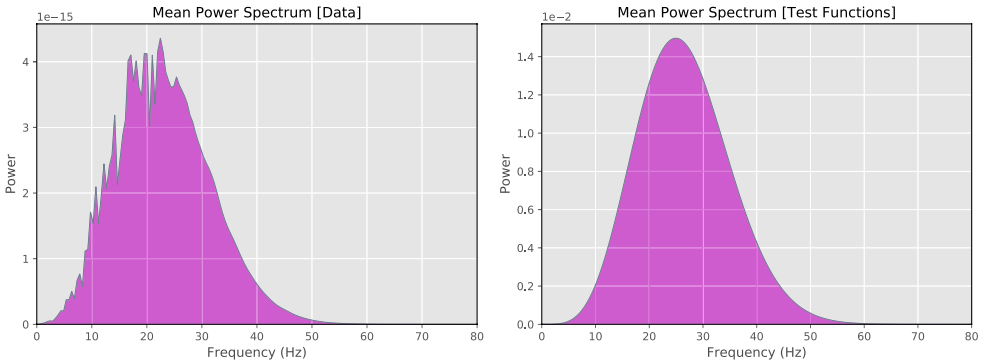

(a) (b)

Figure 9. Power spectra for the two-box imaging experiment. The power spectrum is averaged over all recordings of (a) the scattered wave and (b) the test functions with time dependence given by χ_2.

implementation, indicating that the near-field operator is under-represented. The time to compute the truncated SVD for each implementation is indicated in its respective panel.

Figures 6 and 7 show the obtained reconstructions for the full-aperture and limited-aperture starfish imaging experiments using the three different implementations of the discretized near-field operator. For the truncated implementation, it is clear how the time parameter τ influences the reconstruction of the scatterer boundary. In particular, for three different values of τ, we obtain three completely different images. The time- and frequency-domain implementations that use the full convolution readily give the desired result, which is consistent with the true boundary of the scatterer. As expected, the time-domain implementation fails when τ is set such that the test functions lie outside the convolution interval $[-18, 18]$. In figure 6, the full-aperture acquisition allows the linear sampling method to accurately reconstruct the boundary of the starfish-shaped scatterer, whereas in figure 7, we see the method correctly identified the lower-left ray of the starfish, but largely failed to reconstruct the rest of the scatterer. The diagonal smearing present in figure 7 is characteristic of a limited-aperture acquisition, in which the geometry of a scatterer is not well constrained (a detailed investigation of limited-aperture imaging using the linear sampling method was carried out in [11]). In both imaging experiments, the linear sampling method proved reasonably robust to the noisy data, so long as a small regularization term was added to the solutions (13) and (14).

5.2. Box-shaped scatterers

Our second imaging experiment aims to reconstruct the boundaries of two box-shaped scatterers of different sizes. In this case, the scatterers represent a large contrast in the model wave speed in order to induce strong multiple scattering. Here, the background wave speed is $c_0 = 2$ km s^{-1} and $c = 0.343$ km s^{-1} inside the scatterers (figure 8). As before, we interrogate the scatterers under two different acquisition scenarios. In the first case, we place 24 co-located sources and receivers in a circle around the scatterers, again representing an ideal, full-aperture acquisition setup (figure 8(a)). In the second case, we place 12 co-located sources and receivers along a line at the top of the model, representing a single-sided surface acquisition geometry (figure 8(b)). In both imaging experiments, we sample the model in space with a 51×51 point uniformly spaced sampling grid and interrogate the scatterers using the pulse

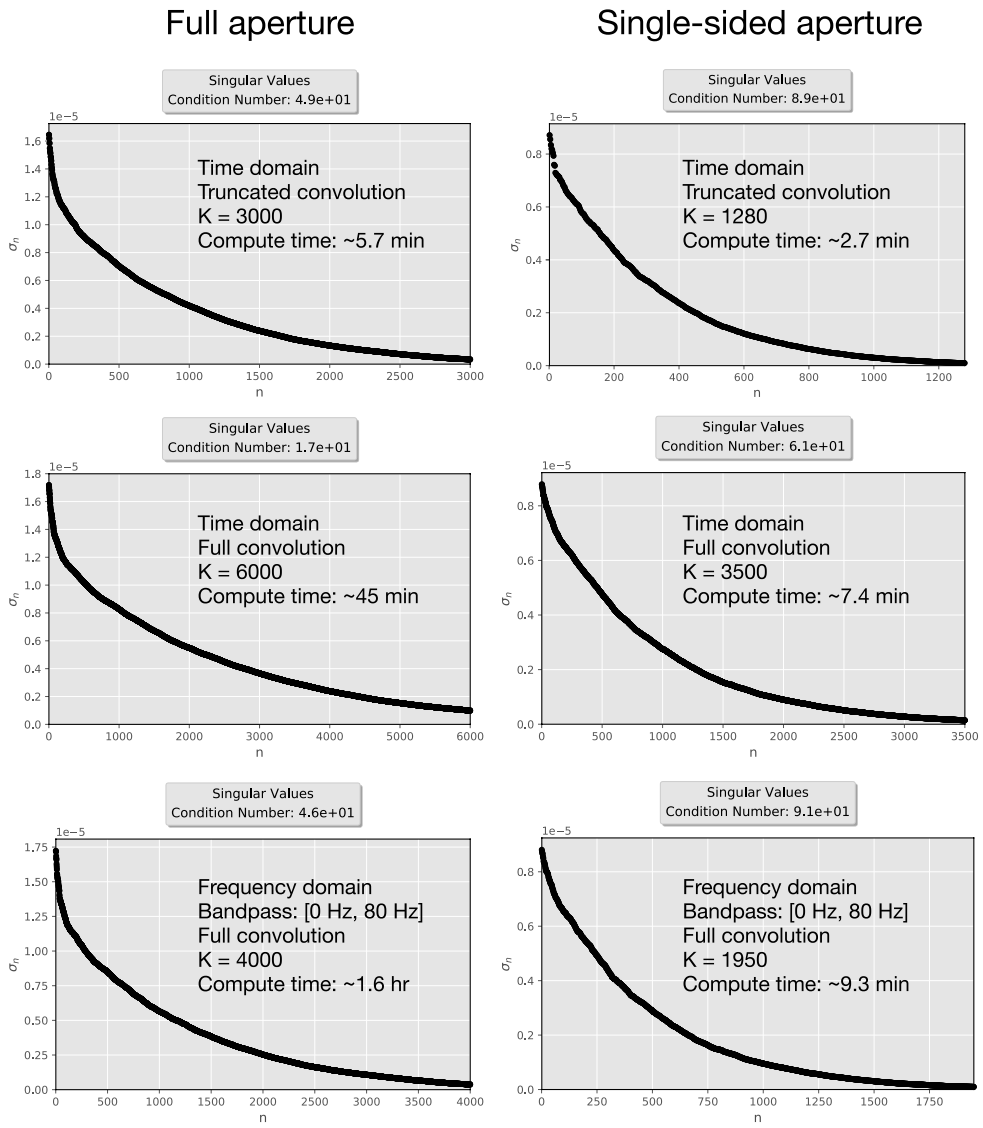

Figure 10. Estimated singular values for the full-aperture (left column) and single-sided (right column) imaging experiments for the two box-shaped scatterers. Each column gives the estimated singular values based on the numerical implementation of the discretized near-field operator. The truncated convolution under-represents the discretized near-field operator, as evidenced by the more rapid decay of the singular values.

function χ_2 with a dominant frequency $\nu = 25$ Hz (the dominant wavelength is shown in figure 8 for scale). The scattered waves are recorded in the time interval [0 s, 2 s] using a step size $\Delta t = 4.0 \times 10^{-2}$ s for a total of $N_t = 501$ time samples. Consequently, the test functions are evaluated in the interval $[-2\text{ s}, 2\text{ s}]$ for the time- and frequency-domain implementations that use the full convolution, and in the interval $[0\text{ s}, 2\text{ s}]$ for the truncated implementation. We do not add any noise for these experiments. The left panels of figure 8 show examples of

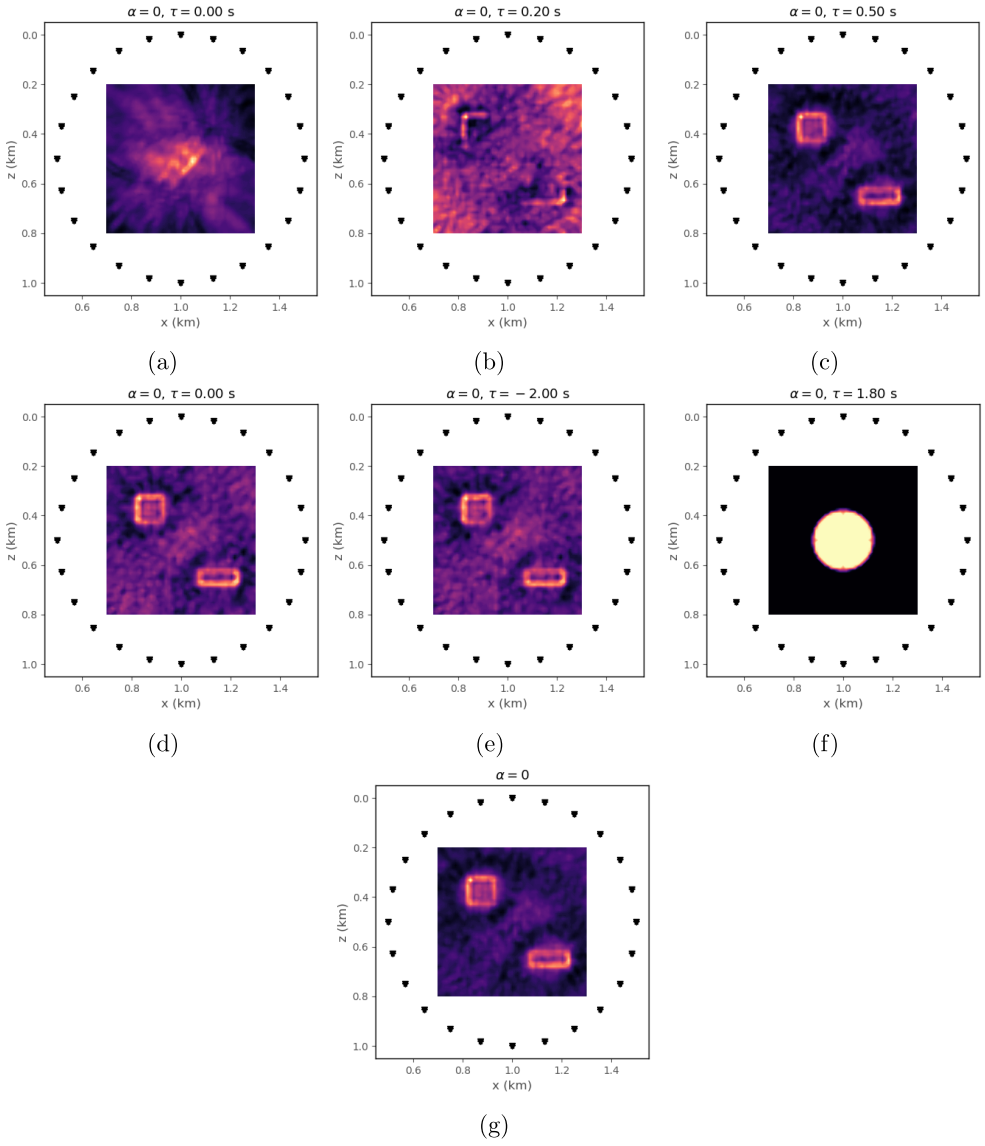

Figure 11. Reconstructions of the two box-shaped scatterers for the full-aperture imaging experiment. ((a)–(c)) Reconstructions based on the truncated convolution in the time domain with $\tau = 0$ s, $\tau = 0.2$ s, and $\tau = 0.5$ s. ((d)–(f)) Reconstructions based on the full convolution in the time domain with $\tau = 0$ s, $\tau = -2$ s, and $\tau = 1.8$ s. When $\tau = 1.8$ s, the test functions lie partially outside the support $[-2\text{ s}, 2\text{ s}]$ and the method fails. (g) Reconstruction based on the frequency-domain approach. The regularization parameter $\alpha = 0$ in all cases.

the recorded scattered waves for the two acquisition geometries. The mean power spectra of the recorded data and test functions are shown in figure 9. Note again that the frequency bands of the data and the test functions overlap significantly, as this ensures an optimal reconstruction of the target. Figure 10 shows the K largest singular values of the truncated SVD used to compute the time and frequency domain solutions (13) and (14), respectively. Again, we

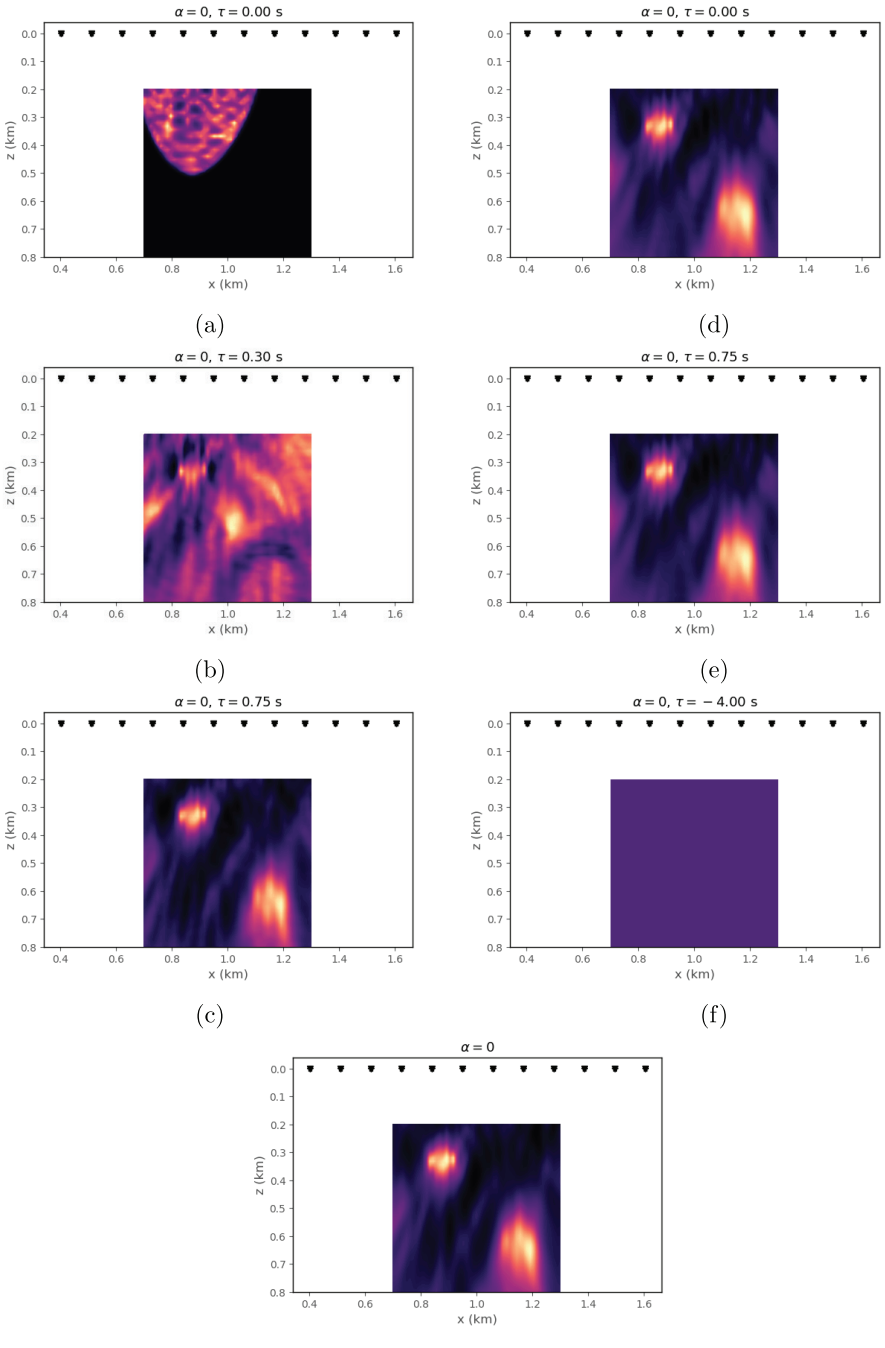

Figure 12. Reconstructions of the two box-shaped scatterers for the single-sided imaging experiment. ((a)–(c)) Reconstructions based on the truncated convolution in the time domain with $\tau = 0$ s, $\tau = 0.3$ s, and $\tau = 0.75$ s. ((d)–(f)) Reconstructions based on the full convolution in the time domain with $\tau = 0$ s, $\tau = 0.75$ s, and $\tau = -4$ s. When $\tau = -4$ s, the test functions lie completely outside the support $[-2\text{ s}, 2\text{ s}]$ and the method fails. (g) Reconstruction based on the frequency-domain approach. The regularization parameter $\alpha = 0$ in all cases.

observe that the singular values decay faster for the truncated implementation, indicating that the near-field operator is under-represented. The time to compute the truncated SVD for each implementation is indicated in its respective panel.

Figures 11 and 12 show the obtained reconstructions for the full-aperture and single-sided imaging experiments for the two box-shaped scatterers using the three different implementations of the discretized near-field operator. Again, we observe that the truncated implementation is strongly dependent on the choice of the time parameter τ to reconstruct the boundaries of the scatterers, whereas the time- and frequency-domain implementations that use the full convolution readily give the desired result. As expected, the time-domain implementation fails when τ is set such that the test functions lie outside the convolution interval $[-2\text{ s}, 2\text{ s}]$. In figure 11, the full-aperture acquisition allows the linear sampling method to accurately reconstruct the boundaries of the box-shaped scatterers, whereas in figure 12, we see the method identified the top-left box, but largely failed to reconstruct the lower-right box. Again, due to the limited-aperture data acquisition, the geometries of the scatterers are not well constrained.

6. Conclusions

We have shown in the appendix that the blowup behavior of solutions to the near-field equation is due to division by a spatially dependent function with compact support that localizes the source of the observed field. This general proof gives valuable insight into how the blowup behavior will depend on different types of source functions, and consequently how the linear sampling method may be applied to other imaging problems. For example, our generalized formulation shows that the linear sampling method could be applied to localizing microseismic events or underground explosions.

We have presented a physical framework in which the time parameter τ corresponds to the focusing time of the Herglotz wave function. Furthermore, our numerical experiments demonstrate how the length of the recorded time interval determines the range of values that τ can assume. Provided the scattered wave is adequately represented in the recorded time interval, our experiments show that the focusing time can be safely assumed zero without loss of generality. The frequency-domain implementation should be preferred for practical applications, as it gives qualitatively similar results as the time-domain implementation and offers additional computational savings.

A practical concern for the linear sampling method is how one can effectively separate the desired scattered wave from the recorded total wave. In principle, one could predict the unperturbed wave field recorded at the receivers and subtract it from the data, but this requires accurate knowledge of the background medium which is not available in many applications. In time-lapse studies, one could subtract the wave fields recorded at different periods in time to obtain the perturbed wave field caused by changes in the medium. However, this application is prone to any errors in the acquisition deployment that influences the repeatability of the experiment. It is therefore of practical interest to understand how the linear sampling method tolerates errors in the acquisition as well as in the assumed background medium.

A promising aspect of the linear sampling algorithm is that it is *embarrassingly parallel*, since the solution of the near-field equation at each sampling point is independent of the solution at every other sampling point. Thus, if one has the computational resources available, the sampling algorithm could easily be distributed over a computing cluster. Our future work will investigate possible approaches to making the linear sampling method more computationally efficient as it is applied to larger-scale imaging problems. Additionally, it would be interesting to compute and visualize the total wave field of the inverse focusing problem, since this

would either validate or reject our interpretation of τ as the focusing time of the Herglotz wave function.

Acknowledgments

We would like to make a special acknowledgment to Yukun Guo for sharing his data set for the starfish experiment, and in particular for his enormous help and patience in getting us started with the linear sampling method. Additionally, we would like to thank two anonymous reviewers whose commentary and constructive feedback greatly helped us enhance the quality and relevance of this paper. This work was funded by the Consortium Project on Seismic Inverse Methods for Complex Structures at the Colorado School of Mines.

Appendix

Here, we give a proof of the blowup behavior of solutions to the near-field equation (8). We introduce two important generalizations that broaden the applicability of the linear sampling method to applications other than localizing scatterers. First, we generalize the notion of recording wave fields due to different known sources to the notion of recording different *realizations* of a wave field that passes through a given medium. For example, $u^s(\cdot,\cdot,\mathbf{x}_s)$ denotes a realization of the scattered wave due to a particular source at $\mathbf{x}_s \in \Gamma_s$. For a different source location, we observe a different realization of u^s. Hence, we replace the idea of integrating over a known acquisition surface Γ_s with the more general idea of integrating over all possible realizations of an observed wave field. This generalization is powerful, since we no longer need to know the source locations $\mathbf{x}_s$. This has important applications in passive imaging, for example, in which unknown, ambient sources interrogate the medium. We denote by Ω the set of all possible realizations of the recorded wave (in practice, of course, we only record a subset of Ω). Second, we generalize the source from a scatterer to any source function S that can be written as countable sum of separable functions in space and time; that is,

$$S(\mathbf{x},t;\mu) = \sum_i R_i(\mathbf{x})\Theta_i(\mathbf{x},t;\mu)$$

for some unknown functions R_i and Θ_i. Here, we assume the source function has terms R_i which depend only on space and not on time or the realization $\mu \in \Omega$ that we measure. Hence, the terms R_i effectively localize the source function and represent its amplitude as a function of space, which in general depends on the physical properties of the source. On the other hand, we allow the time dependence of the source function (given by the functions Θ_i) to depend on both space and realization. For example, the location of a scatterer in a medium is fixed, but the time at which the scatterer acts a source function depends on how the scatterer is interrogated. We assume that each function R_i has compact support $D_i \subset \mathbb{R}^3$ such that sets D_i are pairwise disjoint and that $D = \cup_i D_i$ gives the total spatial support of S. For a given realization $\mu \in \Omega$, expression (9) determines that a wave u generated by such a source has the representation

$$u(\mathbf{x},t;\mu) = \sum_i \int_{\mathbb{R}} \int_{D_i} G_0(\mathbf{x},t-t';\boldsymbol{\eta})R_i(\boldsymbol{\eta})\Theta_i(\boldsymbol{\eta},t';\mu)\,\mathbf{d}\boldsymbol{\eta}\,\mathrm{d}t'.$$

The function w_φ of the inverse problem can be written as a linear combination of all possible realizations of the recorded data:

$$w_\varphi(\mathbf{x},t) = \int_{\mathbb{R}}\int_{\Omega} u(\mathbf{x},t-t';\mu)\varphi(t',\mu)\,\mathrm{d}\mu\,\mathrm{d}t'.$$

The wave fields u and w_φ are given equivalently in the frequency domain by

$$\hat{u}(\mathbf{x};\omega,\mu) = \sum_i \int_{D_i} \hat{G}_0(\mathbf{x};\boldsymbol{\eta},\omega)R_i(\boldsymbol{\eta})\hat{\Theta}_i(\boldsymbol{\eta};\omega,\mu)\,\mathbf{d}\boldsymbol{\eta}, \tag{A.1}$$

and

$$\hat{w}_\varphi(\mathbf{x};\omega) = \int_{\Omega} \hat{u}(\mathbf{x};\omega,\mu)\hat{\varphi}(\omega,\mu)\,\mathrm{d}\mu, \tag{A.2}$$

respectively, where ω is the angular frequency. If we substitute (A.1) into (A.2) and interchange the order of integration, we obtain

$$\hat{w}_\varphi(\mathbf{x};\omega) = \sum_i \int_{D_i} \hat{G}_0(\mathbf{x},\boldsymbol{\eta};\omega)R_i(\boldsymbol{\eta})\left(\int_{\Omega}\hat{\Theta}_i(\boldsymbol{\eta};\omega,\mu)\hat{\varphi}(\omega,\mu)\,\mathrm{d}\mu\right)\mathbf{d}\boldsymbol{\eta}.$$

For notational convenience, we introduce the source functions $\hat{S}_\varphi^{(i)}$ as

$$\hat{S}_\varphi^{(i)}(\boldsymbol{\eta};\omega) := \int_{\Omega}\hat{\Theta}_i(\boldsymbol{\eta};\omega,\mu)\hat{\varphi}(\omega,\mu)\,\mathrm{d}\mu, \tag{A.3}$$

so that the integral representation for $\hat{w}_\varphi$ becomes

$$\hat{w}_\varphi(\mathbf{x};\omega) = \sum_i \int_{D_i} \hat{G}_0(\mathbf{x},\boldsymbol{\eta};\omega)R_i(\boldsymbol{\eta})\hat{S}_\varphi^{(i)}(\boldsymbol{\eta};\omega)\,\mathbf{d}\boldsymbol{\eta}.$$

Suppose we wish to find the contribution to $\hat{w}_\varphi$ from a single point $\mathbf{z}$ in space. We sample the wave field $\hat{w}_\varphi$ using the delta distribution $\delta_{\mathbf{z}} = \delta(\boldsymbol{\eta}-\mathbf{z})$ and obtain

$$\hat{w}_\varphi(\mathbf{x};\mathbf{z},\omega) = \sum_i \int_{D_i} \delta(\boldsymbol{\eta}-\mathbf{z})\hat{G}_0(\mathbf{x},\boldsymbol{\eta};\omega)R_i(\boldsymbol{\eta})\hat{S}_\varphi^{(i)}(\boldsymbol{\eta};\omega)\,\mathbf{d}\boldsymbol{\eta}. \tag{A.4}$$

Note that $\boldsymbol{\eta}$ is the integration variable over the spatial supports D_i of the source function S that generated the wave field u. It follows from (A.4) that if $\mathbf{z}\notin D_i$ for any $i=1,2,\ldots$, then the wave field u is identically zero everywhere, and consequently so is w_φ. Otherwise, if $\mathbf{z}\in D_i$ for some $i=1,2,\ldots$, we have

$$\hat{w}_\varphi(\mathbf{x};\mathbf{z},\omega) = \hat{G}_0(\mathbf{x},\mathbf{z};\omega)R_i(\mathbf{z})\hat{S}_\varphi^{(i)}(\mathbf{z};\omega). \tag{A.5}$$

The test function (7) can be written in the frequency domain as

$$\hat{\Psi}(\mathbf{x};\mathbf{z},\omega) = \hat{G}_0(\mathbf{x},\mathbf{z};\omega)\hat{\zeta}(\omega), \tag{A.6}$$

where the function $\hat{\zeta}\in C^2(\mathbb{R})$ is chosen such that it has overlapping support with the observed field $\hat{u}$. We can obtain the near-field equation be forcing equality between the sampled scattered wave (A.5) and the test function (A.6) on the receiver surface Γ_r:

$$\hat{G}_0(\mathbf{x}_r,\mathbf{z};\omega)R_i(\mathbf{z})\hat{S}_\varphi^{(i)}(\mathbf{z};\omega) = \hat{G}_0(\mathbf{x}_r,\mathbf{z};\omega)\hat{\zeta}(\omega), \quad \mathbf{z}\in D_i,$$

i.e. since $R_i(\mathbf{z})\neq 0$ for $\mathbf{z}\in D_i$,

$$\hat{S}_{\varphi}^{(i)}(\mathbf{z};\omega) = \frac{\hat{\zeta}(\omega)}{R_i(\mathbf{z})}, \quad \mathbf{z} \in D_i. \tag{A.7}$$

Substituting the definition of the source function $\hat{S}_{\varphi}^{(i)}$ (A.3) back into the left-hand side of equation (A.7), we obtain the integral equation

$$\int_{\Omega} \hat{\Theta}_i(\mathbf{z};\omega,\mu)\hat{\varphi}(\omega,\mu)\,\mathrm{d}\mu = \frac{\hat{\zeta}(\omega)}{R_i(\mathbf{z})}, \quad \mathbf{z} \in D_i,$$

or, in the time domain,

$$\int_{\mathbb{R}}\int_{\Omega} \Theta_i(\mathbf{z}, t-t';\mu)\varphi(t',\mu)\,\mathrm{d}\mu\,\mathrm{d}t' = \frac{\zeta(t)}{R_i(\mathbf{z})}, \quad \mathbf{z} \in D_i. \tag{A.8}$$

Note that if the observed field u has finite energy (i.e. is square integrable in the sense of Lebesgue), so does its source function S. In particular, the functions Θ_i are square integrable. Therefore, the integral operator on the left-hand side of equation (A.8) admits a singular-value decomposition [18]. If we denote this singular-value decomposition by $(\sigma_n, \phi_n, \psi_n)$, where σ_n are the singular values and ϕ_n and ψ_n are the corresponding left- and right-singular vectors, respectively, then a solution to equation (A.8) can be written as

$$\varphi_{\mathbf{z}} = \sum_{n=1}^{\infty} \frac{1}{\sigma_n} \left\langle \phi_n, \frac{\zeta}{R_i} \right\rangle_{L^2(\mathbb{R})} \psi_n,$$

where $\langle\cdot,\cdot\rangle_{L^2(\mathbb{R})}$ denotes the standard L^2 inner product. It follows that in the limit as $\mathbf{z} \to \partial D_i$, the function $R_i(\mathbf{z}) \to 0$ and the coefficients $\langle \phi_n, \zeta R_i^{-1}\rangle_{L^2(\mathbb{R})}$ become uniformly unbounded (i.e. unbounded for all $n \in \mathbb{N}$). In fact, the function $R_i(\mathbf{z}) = 0$ for all $\mathbf{z} \in \mathbb{R}^3 \setminus \overline{D}_i$. Thus, any solution $\varphi_{\mathbf{z}}$ to equation (A.8)—and consequently to the near-field equation (8)—becomes unbounded as $\mathbf{z} \to \partial D_i$, and remains unbounded in general for all $\mathbf{z} \in \mathbb{R}^3 \setminus \overline{D}$. Thus, the blowup behavior of solutions to the near-field equation is due to division by the spatially dependent functions R_i with compact support D_i.

Note that if we do not know the background medium exactly, then we cannot write the test function $\Psi_{\mathbf{z}}$ using expression (A.6), since the unperturbed Green function G_0 is unknown. Suppose instead we approximate the Green function by another function H. Then equation (A.7) becomes

$$\hat{S}_{\varphi}^{(i)}(\mathbf{z};\omega) = \frac{\hat{H}(\mathbf{x}_r,\mathbf{z};\omega)\hat{\zeta}(\omega)}{R_i(\mathbf{z})\hat{G}_0(\mathbf{x}_r,\mathbf{z};\omega)},$$

which is a *deconvolution* of H and G_0 in the frequency domain.

ORCID iDs

Aaron C Prunty https://orcid.org/0000-0003-2822-5220
Roel K Snieder https://orcid.org/0000-0003-1445-0857

References

[1] Colton D and Kirsch A 1996 *Inverse Problems* **12** 383

[2] Colton D, Piana M and Potthast R 1997 *Inverse Problems* **13** 1477
[3] Colton D and Kress R 2013 *Inverse Acoustic and Electromagnetic Scattering Theory* vol 93, 3rd edn (New York: Springer)
[4] Cakoni F and Colton D 2014 *A Qualitative Approach to Inverse Scattering Theory* (New York: Springer)
[5] Arens T 2003 *Inverse Problems* **20** 163
[6] Arens T *et al* 2009 *J. Integral Equ. Appl.* **21** 179–202
[7] Chen Q, Haddar H, Lechleiter A and Monk P 2010 *Inverse Problems* **26** 085001
[8] Guo Y, Monk P and Colton D 2013 *Inverse Problems* **29** 095016
[9] Haddar H, Lechleiter A and Marmorat S 2014 *Appl. Anal.* **93** 369–90
[10] Khaji N and Manshadi S D 2015 *Comput. Struct.* **153** 36–48
[11] Guo Y, Monk P and Colton D 2016 *Appl. Anal.* **95** 1599–615
[12] Catapano I, Crocco L and Isernia T 2007 *IEEE Trans. Antennas Propag.* **55** 1431–6
[13] Fink M 1993 *J. Phys. D: Appl. Phys.* **26** 1333
[14] Roux P and Fink M 2000 *J. Acoust. Soc. Am.* **107** 2418–29
[15] Calvo H L, Jalabert R A and Pastawski H M 2008 *Phys. Rev. Lett.* **101** 240403
[16] Lechleiter A and Monk P 2015 *Numer. Methods PDE* **31** 517–40
[17] Tikhonov A N, Goncharsky A, Stepanov V and Yagola A G 2013 *Numerical Methods for the Solution of Ill-Posed Problems* vol 328 (New York: Springer)
[18] Hansen P C 2010 *Discrete Inverse Problems: Insight and Algorithms* vol 7 (Philadelphia, PA: SIAM)
[19] Lehoucq R B, Sorensen D C and Yang C 1998 *ARPACK Users' Guide: Solution of Large-Scale Eigenvalue Problems with Implicitly Restarted Arnoldi Methods* vol 6 (Philadelphia, PA: SIAM)